Numerical Simulations of Orographic Convection across Multiple Gray Zones

DANIEL J. KIRSHBAUM

Department of Atmospheric and Oceanic Sciences, McGill University, Montreal, Quebec, Canada

(Manuscript received 5 February 2020, in final form 23 July 2020)

ABSTRACT: Idealized simulations are used to determine the sensitivity of moist orographic convection to horizontal grid spacing Δ_h. In simulated mechanically (MECH) and thermally (THERM) forced convection over an isolated ridge, Δ_h is varied systematically over both the deep-convection ($\Delta_h \sim 10$–1 km) and turbulence ($\Delta_h \sim 1$ km–100 m) gray zones. To aid physical interpretation, a new parcel-based bulk entrainment/detrainment diagnosis for horizontally heterogeneous flows is developed. Within the deep-convection gray zone, the Δ_h sensitivity is dominated by differences in parameterized versus explicit convection; the former initiates convection too far upstream of the ridge (MECH) and too early in the diurnal heating cycle (THERM). These errors stem in part from a large underprediction of parameterized entrainment and detrainment. Within the turbulence gray zone, sensitivities to Δ_h arise from the representation of both subcloud- and cloud-layer turbulence. As Δ_h is decreased, MECH exhibits stronger cloud-layer entrainment to enhance the convective mass flux M_{co}, while THERM exhibits stronger detrainment to suppress M_{co} and delay convection initiation. The latter is reinforced by increased subcloud turbulence at smaller Δ_h, which leads to drying and diffusion of the central updraft responsible for initiating moist convection. Numerical convergence to a robust solution occurs only in THERM, which develops a fully turbulent flow with a resolved inertial subrange (for $\Delta_h \leq 250$ m). In MECH, by contrast, turbulent transition occurs within the orographic cloud, the details of which depend on both physical location and Δ_h.

KEYWORDS: Convection; Mesoscale processes; Boundary layer; Mesoscale models; Mountain meteorology

1. Introduction

As computer power increases, so does the refinement of grids in weather and climate prediction models. In the process, certain atmospheric phenomena that were previously unresolved become partially to completely explicit. For a given phenomenon, the interval of horizontal grid spacings Δ_h over which this transition occurs is termed its "gray zone" (e.g., Wyngaard 2004; Chow et al. 2019). The gray zone is dictated by the physical scale of the process and the effective resolution of the model, the latter of which exceeds Δ_h due to large numerical error and/or diffusion at poorly resolved scales (e.g., Skamarock 2004; Ricard et al. 2013). A process can only be resolved if its dominant length scale exceeds the effective grid resolution.

The gray zone for deep moist convection (DMC) ranges from $\Delta_h \sim O(10)$ km, the characteristic cloud diameter, down to $O(1)$ km (e.g., Field et al. 2017). Seamlessly representing DMC across this zone requires scale-aware cumulus parameterizations, where the parameterized transport is a function of Δ_h. At $O(1)$ km, simulations are often termed "convection permitting" (CP) because explicit convection can readily develop on the model grid. CP grids, however, cannot resolve most turbulent eddies within the planetary boundary layer (PBL), and thus a PBL parameterization is often used to represent their effects.

PBL parameterizations are not used in large-eddy simulations (LES), where larger PBL eddies and part of the inertial subrange are resolved, and a subgrid turbulence closure is used to complete the forward energy cascade. Analogous to the deep-convection problem, the turbulence gray zone extends from scales of $\Delta_h \sim O(1)$ km, where PBL turbulence is mostly parameterized, down to the scale at which the turbulence is mostly explicit. While the latter depends on z_i (e.g., Honnert et al. 2011; Shin and Hong 2013; Beare 2014), it is often taken as $\Delta_h \sim O(100)$ m, which suffices to resolve the larger eddies in a convective PBL with $z_i \approx 1$ km (Honnert 2016).

In moist flows, turbulence may also be driven by sharp gradients across cloud edges (among other things), which induces mixing between clouds and their surroundings. According to Craig and Dornbrack (2008), the necessary Δ_h to resolve this mixing is determined by the smaller of two scales: the cloud diameter and a buoyancy length scale. Both of these scales are typically several hundred meters or more, and thus $\Delta_h \sim 50$ m often suffices.

As with deep convection, seamless representation of turbulent mixing within the turbulence gray zone requires scale-aware turbulence closures. Although traditional subgrid turbulence schemes are scale-aware (e.g., Smagorinsky 1963; Deardorff 1980), they were developed for use in LES, where Δ_h lies within the inertial subrange. However, today's convection-permitting numerical weather prediction (NWP) models with $\Delta_h \sim O(1)$ km generally do not to satisfy this condition. Thus, new turbulence closures have been proposed in recent years to account for the spectral gap between Δ_h and the inertial subrange (e.g., Moeng et al. 2010; Boutle et al. 2014; Shi et al. 2018, 2019b,a).

Because cumuli form at or near the grid scale in convection-permitting forecast models, their representation is prone to error. Thus far, however, systematic trends in these the errors have been difficult to determine. Of the studies that have

Corresponding author: Daniel J. Kirshbaum, daniel.kirshbaum@mcgill.ca

DOI: 10.1175/JAS-D-20-0035.1

simulated convection over a wide range of Δ_h, some have found the bulk properties of convection (e.g., convective mass flux and precipitation) to reach robust, numerically converged solutions for $\Delta_h \sim O(1)$ km and below (e.g., Weisman et al. 1997; Clark et al. 2012; Langhans et al. 2012; Verrelle et al. 2015; Panosetti et al. 2019). However, others have found bulk properties to continue varying well into the turbulence gray zone (e.g., Bryan et al. 2003; Warren et al. 2014; Varble et al. 2019). Moreover, cloud-size distributions tend not to converge at all with decreased Δ_h, instead just shifting to progressively smaller sizes (e.g., Hanley et al. 2015; Panosetti et al. 2019).

One may reasonably expect that, in convection-permitting NWP, sensitivities to Δ_h may stem from the representation of subgrid mixing processes within the cloud layer. However, processes within the underlying subcloud layer may also play a decisive role. In a NWP case study of a quasi-stationary convective system over the southwest U.K. peninsula, Warren et al. (2014) found that simulated DMC was delayed (relative to observations) by around 3 h at $\Delta_h = 1.5$ km. This error was eliminated by decreasing Δ_h to 500 m, which produced an amplified sea-breeze convergence line that initiated DMC more readily. Furthermore, in LES experiments of convection initiation over a mesoscale convergence line, Tang and Kirshbaum (2020) found that cloud-top heights and precipitation progressively decreased as Δ_h was reduced from 500 to 125 m, in part due to increased turbulent diffusion of the narrow subcloud updraft at smaller Δ_h.

Two common situations in which DMC occurs are orographic in nature: (i) mechanically forced ascent of impinging flow and (ii) elevated thermal circulations driven by differential heating (Kirshbaum et al. 2018). Schwitalla et al. (2008) conducted hindcasts of mostly mechanically forced convection events over the Black Forest in southwestern Germany and identified a robust bias in simulations with parameterized convection. This bias, termed the ''windward lee'' effect, manifested as overly heavy precipitation over the windward (western) slope and too light precipitation over the lee (eastern) slope. These errors largely vanished in CP runs with $\Delta_h = O(1)$ km. In idealized simulations of thermally forced convection over an idealized double-ridge system, Panosetti et al. (2016) found that DMC initiation occurred more readily at $\Delta_h = 1$ km than at $\Delta_h = 200$ m, due to increased turbulent mixing with the free troposphere drying the PBL and delaying convective initiation in the latter case.

The above studies on the Δ_h sensitivities of orographic convection have only considered limited subsets of a larger problem. Namely, they focus on either the deep-convection or the turbulence gray zone, in the context of either mechanically forced or thermally forced convection. Herein, both mechanisms of orographic convection are evaluated across both the deep-convection and the turbulence gray zones, using a consistent numerical framework. The remainder of this manuscript is organized as follows: section 2 describes the numerical model and setups for both the mechanically and thermally driven experiments. Sections 3 and 4 analyze the resolution sensitivities for mechanically and thermally driven convection, respectively. Additional physical interpretation of the results is provided in section 5, and conclusions are drawn in section 6.

2. Model setup

The Cloud Model 1 (CM1; Bryan and Fritsch 2002), version 19, is used for the numerical experiments. This idealized cloud model is compressible, nonhydrostatic, and fully nonlinear. The experiments use third-order Runge–Kutta time integration, with a split time step for stability of acoustic modes. Advection is fifth-order in both the horizontal and vertical, using a weighted essentially nonoscillatory (WENO) scheme for scalars. The Morrison two-moment liquid–ice cloud microphysics scheme (Morrison et al. 2009) is used in all simulations with a fixed cloud droplet concentration of 250 cm^{-3} for simplicity.

In crossing the deep-convection and turbulence gray zones, the cumulus and subgrid turbulence parameterizations are critically important. These schemes need a certain degree of scale awareness to adjust to changes in the representation of the process on the model grid. In designing the experiments, we evaluated whether to use the most cutting-edge scale-aware parameterizations available versus other, more traditional ones that currently enjoy widespread use. We have opted for the latter, mainly to provide a benchmark analysis that highlights areas in need of improvement and drives future efforts to develop and test parameterizations designed for each gray zone.

In mesoscale cloud simulations, turbulence may be generated both inside the PBL and above the PBL within clouds (or other dynamical processes). As discussed in section 1, the characteristic length scales of these phenomena may differ, and thus a given turbulence closure may struggle to simultaneously represent both. Two 3D LES turbulence closures are available in CM1, a Smagorinsky (1963) first-order closure and the 1.5-order turbulence kinetic energy (TKE) closure of Deardorff (1980). Also available is the 1D nonlocal PBL parameterization of Hong et al. (2006), which can be extended to 3D with a Smagorinsky (1963) closure in the horizontal.

Fiori et al. (2010) studied the impact of the subgrid turbulence scheme on the simulation of supercells in idealized flows with no PBL across the turbulence gray zone. The schemes under evaluation were very similar to those described above. As Δ_h was progressively decreased, the simulated convection converged to that of a $\Delta_h = 200$ m reference case only when using a 3D LES closure. Accordingly, we choose Deardorff (1980) as the default in our simulations. This scheme is scale aware in that the subgrid-scale eddy heat flux and turbulent dissipation coefficients both depend on $\Delta s = (\Delta_h^2 \Delta_v)^{1/3}$, where Δ_v is the vertical grid spacing. This local LES closure, however, may struggle to represent PBL development due to an overly small turbulent length scale and the neglect of nonlocal, countergradient fluxes (e.g., Ricard et al. 2013) Therefore, the 3D version of the Hong et al. (2006) PBL parameterization is also critically evaluated in section 2b.

The Kain–Fritsch (KF) cumulus parameterization (Kain 2004) is used to represent subgrid moist convection for $\Delta_h \geq 5$ km. This scheme contains a Δ_h sensitivity in the convective adjustment time scale ($\tau = \Delta_h/U$, where U is a mean lower-tropospheric horizontal wind speed). Thus, as Δ_h is decreased, the convective adjustment proceeds more rapidly, which contrasts with the expectation for parameterized convection to weaken as explicit convection increases at smaller Δ_h. Although modifications to τ have been proposed to address this issue

(Bullock et al. 2015; Wang et al. 2019), we use the original formulation in Kain (2004) given its widespread use. We select the user option in the KF scheme to transfer parameterized condensate back to the resolved grid rather than falling immediately to the ground, based on its superior performance in Cannon (2012).

All simulations use a Cartesian grid with a domain size of $L_x = 360$ km, $L_y = 60$ km, and $L_z = 20$ km, and are integrated for 6 h. A Gaussian ridge given by $h = h_m e^{-(x/a)^2}$, where h_m = 1 km and $a_m = 20$ km are the mountain height and half-width, is placed at the domain center ($x = 0$ km). Given the y-invariant ridge geometry, larger-scale flow variations are confined to the x–z plane, with the narrow y dimension included to permit three-dimensional circulations and facilitate statistical analysis at each x–z grid point. The very smooth form of the ridge, which contrasts with the rugged ridges found in reality, is used for simplicity; it isolates the impacts of atmospheric, rather than terrain, resolution on the representation of orographic cumuli.

The lateral boundary conditions are periodic and the upper boundary is closed, with a 8-km-deep Rayleigh damping layer beneath the model top. The vertical grid, which is held fixed in all experiments, uses $\Delta_v = 100$ m from the surface up to 6 km, stretches to 400 m at 12 km, and remains constant at 400 m above, giving 104 levels. The horizontal grid spacing Δ_h is uniform for each experiment, but is systematically varied in different experiments from near the top end of the deep-convection gray zone ($\Delta_h = 10$ km) to the bottom end of the turbulence gray zone ($\Delta_h = 62.5$ m), with six values in between (5 km, 2 km, 1 km, 500 m, 250 m, and 125 m). In all simulations, uniformly distributed random potential temperature θ perturbations with a maximum amplitude of 0.1 K are added to the initial state at all grid points to seed convective motions. For $\Delta_h = 250$ m, an ensemble of five simulations with different random perturbation fields is conducted to estimate the uncertainty of the numerical solution.

To facilitate the entrainment and detrainment calculations in sections 3b and 4b, the simulations use both inline parcel-trajectory analysis and passive-tracer analysis. The parcels are initialized on a regular 1 km × 1 km grid in the horizontal, with 200 m spacing in the vertical from the surface to 10 km above ground level (AGL), giving 1 080 000 parcels in total. The properties of each parcel, including location, velocity, and thermodynamic information, are written to file every 1 min. Two passive tracers are also defined, with the first varying linearly from a maximum value of 1 g kg^{-1} at sea level to zero at 10 km (and remaining zero above) and the second varying linearly from zero at the surface to 1 g kg^{-1} at 10 km (and remaining constant above). These initial vertical gradients allow for diverse tracer concentrations within the parcels, which facilitates the quantification of cloud mixing processes.

a. *Mechanically forced convection*

The first set of simulations involves flow of moist, conditionally unstable air over the ridge, broadly representing cool-season postfrontal maritime flow in the midlatitudes (e.g., Purnell and Kirshbaum 2018). For ease of reference, each simulation is uniquely named by the prefix "MECH" plus the grid spacing (e.g., MECH-10km for the $\Delta_h = 10$ km case and MECH-62m for the $\Delta_h = 62.5$ m case). The initial sounding is characterized by a surface temperature of $T_s = 285$ K, a Brunt–Väisälä frequency of $N = 0.01$ s^{-1} below the tropopause ($z_t = 10$ km) and 0.02 s^{-1} above, a relative humidity with respect to liquid water (RH$_l$) of 90% from the surface to 2.5 km, decreasing linearly to 30% to the tropopause, and remaining 30% above (Fig. 1a). The convective available potential energy (CAPE) and convective inhibition (CIN) for a mean-layer (0–500 m) parcel are 177 and 6 J kg^{-1}, respectively.

The initial zonal wind speed U is uniformly 10 m s^{-1}, yielding a dry nondimensional mountain height of $M = Nh_m/U = 1$ that would suggest moderate upstream blocking in a dry atmosphere (e.g., Smith 1989). However, latent-heat release within the orographic cap cloud partially counteracts that effect (e.g., Jiang 2003), permitting low-level cross-barrier flow. This flow reaches a quasi-steady state by around 3 h of model integration (as will be shown). For simplicity, the lower boundary is free-slip and unheated, and no surface layer or boundary layer parameterizations are used. Although such PBL-free simulations are common in idealized studies of orographic convection (e.g., Kirshbaum and Durran 2004; Fuhrer and Schär 2005; Miglietta and Rotunno 2009), they are inherently unrealistic because all real-world flows possess a turbulent PBL. The implications of this idealization are discussed in section 5.

b. *Thermally forced convection*

The second set of simulations involves moist and initially quiescent ($U = 0$ m s^{-1}) flow that, in response to surface heating, develops a local thermal circulation over the ridge. The naming convention is the same as before, except for "MECH" being replaced by "THERM." The initial flow (Fig. 1b) mimics a late-spring morning sounding in the northern U.S. Great Plains (e.g., Fig. 12 of Soderholm et al. 2014), with $T_s = 290$ K and a four-layer stability structure: (i) a nocturnal inversion over 0–500 m with $N = 0.02$ s^{-1}, (ii) a conditionally unstable layer over 500–4000 m with $N = 0.009$ s^{-1}, (iii) a slightly moist stable layer from 4 km to $z_t = 12$ km with $N_m = 0.005$ s^{-1}, where N_m is the moist Brunt–Väisälä frequency (Durran and Klemp 1982), and (iv) a stable stratosphere ($N = 0.02$ s^{-1}). The RH$_l$ profile is piecewise-linear, ranging from RH$_l$ = 90% (surface), to 60% ($z = 500$ m), to 50% ($z = 4$ km), and to 20% ($z \geq z_t$). Although the lapse rate of the third layer is defined with respect to a moist adiabat, the layer is initially unsaturated. The initial mean-layer CAPE and CIN are 247 and 162 J kg^{-1}, respectively.

Thermal forcing is provided by horizontally uniform surface sensible and latent-heat fluxes, both equal to 200 W m^{-2}, applied over the duration of the simulations. This forcing, which is accompanied by a no-slip surface, causes a convective PBL to develop and deepen over time. In addition, the baroclinicity generated by surface heating over sloping terrain drives a thermal circulation, with surface-based up-mountain flow converging over the mountain crest (Kirshbaum 2013). This central updraft serves as the lifting mechanism for convection initiation.

On grids with $\Delta_h \lesssim 500$ m, the convective PBL grows explicitly and realistically through the action of resolved turbulent eddies. However, on coarser grids with $\Delta_h \sim O(1–10)$ km,

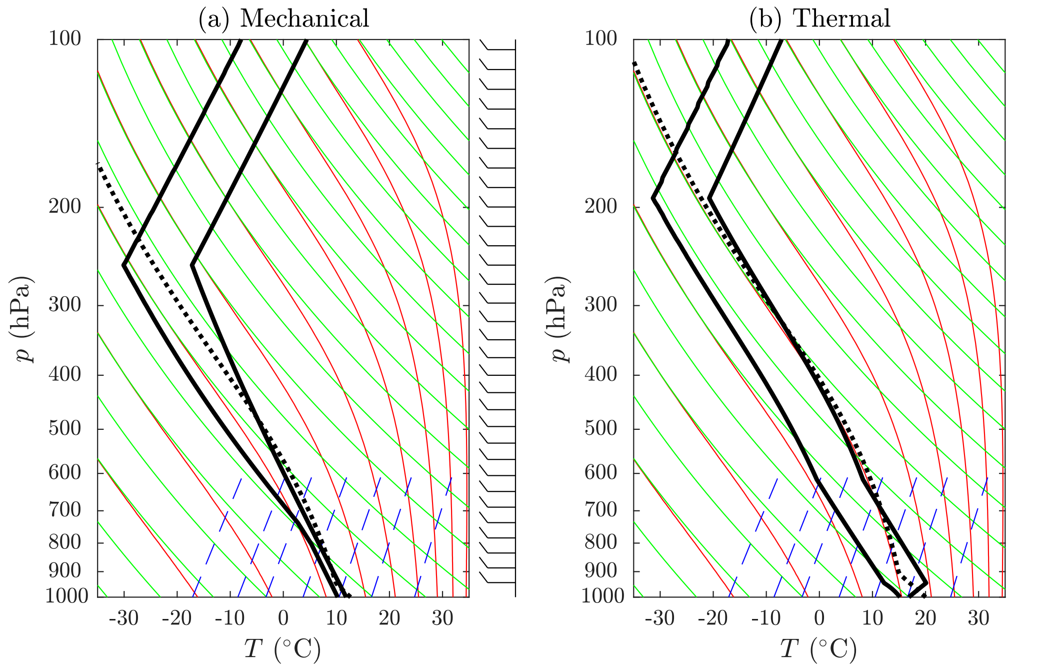

FIG. 1. Skew T–log$p$ profiles of initial conditions for the (a) mechanically and (b) thermally driven simulations. Full wind barbs correspond to $10\,\mathrm{m\,s^{-1}}$, and black dashed lines indicate the temperature of the mean-layer (0–500 m) adiabatically lifted parcel.

PBL eddies are poorly resolved and typically parameterized in NWP models. As discussed in section 2, boundary layer transports in CM1 may be represented by a 3D LES closure (e.g., Deardorff 1980) or a nonlocal 1D PBL scheme (Hong et al. 2006), optionally accompanied by horizontal mixing along model surfaces based on Bryan and Rotunno (2009).

To evaluate the Δ_h sensitivity of PBL development over simple, flat terrain, y-averaged profiles of θ and water vapor mixing ratio q_v are presented at a location far from the mountain ridge ($x = -120$ km), at 3 h in Fig. 2. Profiles are shown for the Deardorff (1980) LES closure as well as a THERM-10km variant using the 1D Hong et al. (2006) PBL scheme coupled with horizontal mixing (THERM-10km-PBL). For $\Delta_h \leq 125$ m, the PBLs are nearly identical, suggesting numerical convergence to a statistically robust reference solution. While the PBL grows far too rapidly in THERM-10km-PBL, it grows too slowly in

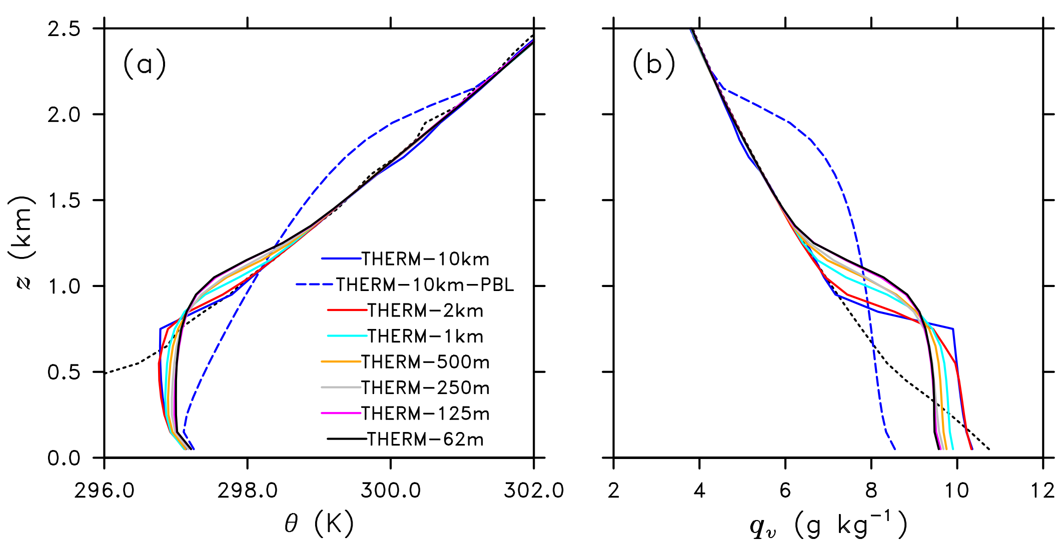

FIG. 2. Profiles of (a) θ and (b) q_v over flat terrain at $x = -120$ km, y-averaged at 3 h of time integration, for various THERM simulations. For reference, dotted black lines show the corresponding initial profiles.

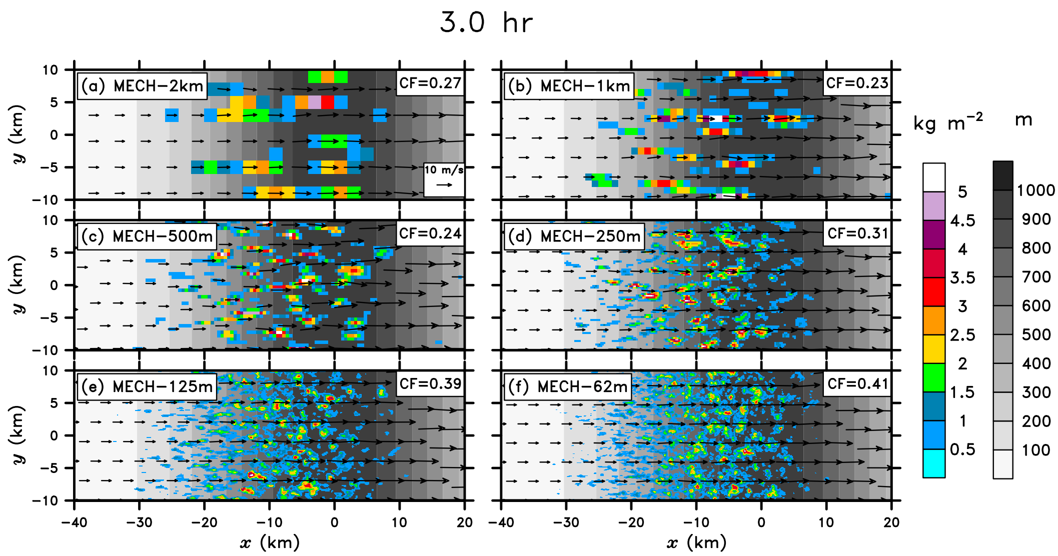

FIG. 3. Cloud water path (CWP; color fill) and lowest-model-level wind vectors at 3 h for the MECH simulations at different horizontal grid spacings, over a subset of the model domain. The underlying terrain is shown in grayscale, and the cloud fraction (CF, the fraction of pixels with CWP $> 0.5\,\mathrm{kg\,m^{-2}}$ over $-30 \le x \le 0$ km) is shown in the upper-right corner.

THERM-10km due to the absence of resolved eddies. However, the latter resembles the THERM-62m case far more closely than does the former. Therefore, to focus our analysis on cases with reasonably similar PBL development, we henceforth use the 3D Deardorff (1980) closure exclusively. Errors stemming from the slower PBL growth in the coarser-resolution cases are estimated in sections 4d and 5.

3. Mechanical forcing

A qualitative picture of the sensitivity of cloud properties to Δ_h in the convection-permitting (CP; $\Delta_h \le 2$ km) MECH cases is provided by snapshots of cloud water path (CWP; vertically integrated liquid/ice hydrometeor mass) at 3 h (Fig. 3). For ease of viewing, only a portion of the computational domain is shown. The two convection-parameterizing cases are omitted because their maximum CWP fails to exceed the smallest contour level in the plot. As Δ_h decreases in the CP simulations with $\Delta_h \le 2$ km, individual cloud objects over the windward slope decrease in size but collectively occupy larger surface areas to yield increased cloud fractions (particularly for $\Delta_h \le 500$ m).

a. Bulk convergence

Following Panosetti et al. (2019), the term "bulk convergence" refers to a systematic reduction in the marginal changes in bulk flow properties as Δ_h is progressively decreased. These properties include mean and/or integrated statistics over the full cumulus ensemble. The degree of convergence will be assessed qualitatively based on evaluation of several metrics. If a given set of experiments are numerically convergent, there must exist a Δ_h at which further grid refinement will no longer noticeably change the statistical results. This Δ_h is henceforth termed the "robustness" scale.

To evaluate bulk convergence, time series of maximum cloud-top height and volume-integrated cloud-core vertical mass flux ($\int_V M_{\mathrm{co}}dV$, where V is volume) over $x \in [-60, 0]$ km, along with y-averaged surface precipitation rate R over $x \in [-60, 20]$ km, are presented in Fig. 4. This analysis sums over both parameterized (if relevant) and resolved contributions, and, for the MECH-250m case, shows a gray-shaded range depicting the minimum and maximum values of the five-member ensemble.

All three abovementioned metrics show a strong sensitivity to Δ_h. The cloud-top height decreases from over 7 km in the parameterized, or PAR, cases (MECH-10km and MECH-5km) to 3–5 km in the CP cases (Fig. 4a). Among the latter group, a quasi-steady state is reached by around 3 h, after which the cloud tops remain nearly fixed at around 4 km. At later times, however, cloud tops increase to around 7 km in MECH-1km and MECH-500m as an elevated mountain-wave cloud migrates upstream into the analysis region. The mass flux and R are also larger in the PAR cases than in the CP cases at early stages, but later decrease substantially. Over the 3–6-h period, the mass flux in the PAR cases falls below that in the corresponding CP cases while R remains slightly larger (Figs. 4b,c).

Although the differences between PAR ($\Delta_h \ge 5$ km) and CP ($\Delta_h \le 2$ km) simulations dominate the above comparison, notable variations are also found among the CP cases. Focusing on the 3–6-h quasi-steady period, the cloud-top height and R are generally very similar in all of these cases, with the exception of relatively small R at later times for MECH-2km and MECH-1km. In contrast, the mass flux progressively increases as the grid is refined, with an increase of about 30% from MECH-2km to MECH-62m. The onset of bulk convergence appears to occur at around $\Delta_h = 1$ km, beyond which the

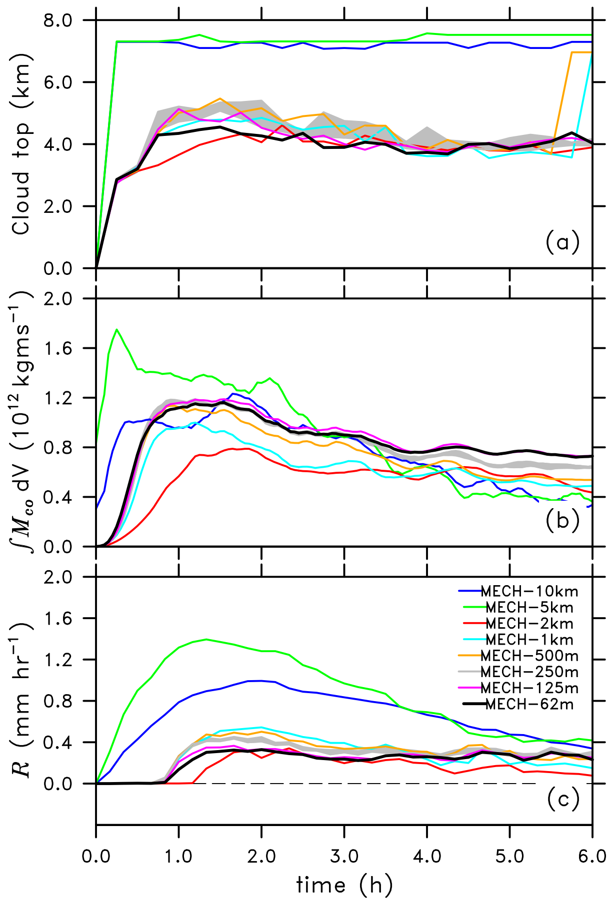

FIG. 4. Variation of bulk properties among the MECH simulations: (a) maximum cloud-top height over $x \in [-60, 0]$, (b) volume-integrated convective mass flux, and (c) area-averaged rainfall over $x \in [-60, 20]$. The gray-shaded area for the MECH-250m case indicates the range of values in the corresponding five-member ensemble.

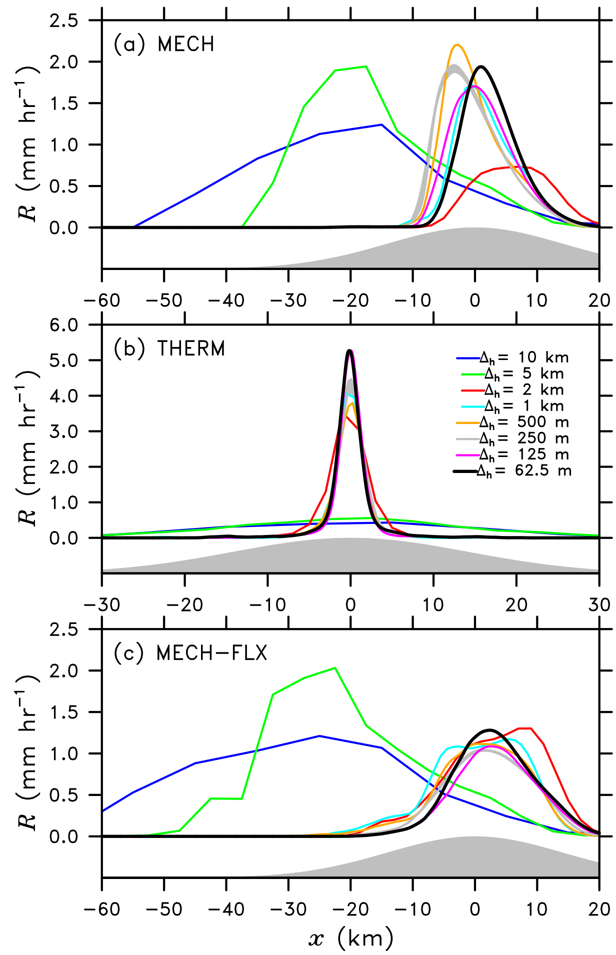

FIG. 5. Time-averaged surface precipitation rates for the (a) MECH simulations over 3–6 h, (b) THERM simulations over 0–6 h, and (c) MECH-FLX simulations, again over 3–6 h. The gray-shaded area for the MECH-250m case indicates the range of values in the corresponding five-member ensemble.

solutions become increasingly similar. The solutions become largely indistinguishable for $\Delta_h \leq 125$ m, at which point robustness is reached. For both mass flux and R, the spread of the 250-m ensemble is much smaller than the magnitude of Δ_h sensitivity, suggesting that the latter is robust and cannot be explained by random variability.

Major differences in spatial precipitation distribution, averaged in y and in time over 3–6 h, are found across the MECH experiments (Fig. 5a). Relative to the CP cases, the PAR runs exhibit an upstream shift, with a broad distribution spread over windward areas but minimal precipitation over the crest and into the lee, thus reproducing the windward–lee effect (Schwitalla et al. 2008). In the CP cases, by contrast, the precipitation is focused in a narrower distribution maximized near the crest in all but MECH-2km, which forms only light precipitation over the lee slope. Unlike the other bulk metrics in Fig. 4, the precipitation distribution does not numerically converge as Δ_h is decreased; it undergoes obvious positional shifts all the way down to $\Delta_h = 62.5$ m.

b. Entrainment and detrainment

Entrainment and detrainment refer to the ingestion of surrounding air into clouds and the expulsion of cloudy air into the surroundings, respectively. In the preceding, the term "clouds" can refer to clouds themselves or to the buoyant cores within clouds. Different methods to calculate entrainment/detrainment have been proposed in the literature. Some of these methods are "direct," in that they directly calculate mass exchange across cloud surfaces (Romps 2010; Dawe and Austin 2011). Other "bulk" methods evaluate statistics over a cloud ensemble, with entrainment taken as the mean degree of cloud dilution by environmental air and detrainment the mean loss of cloudy air to the environment (e.g., Betts 1975; Siebesma and Cuijpers 1995, hereafter SC95). Bulk methods are more commonly used in practice due to their relative simplicity and applicability to both observations and numerical simulations. Moreover, they are analogous to entrainment/detrainment calculations in bulk mass-flux cumulus schemes like KF (e.g., de Rooy et al. 2013). Thus, to

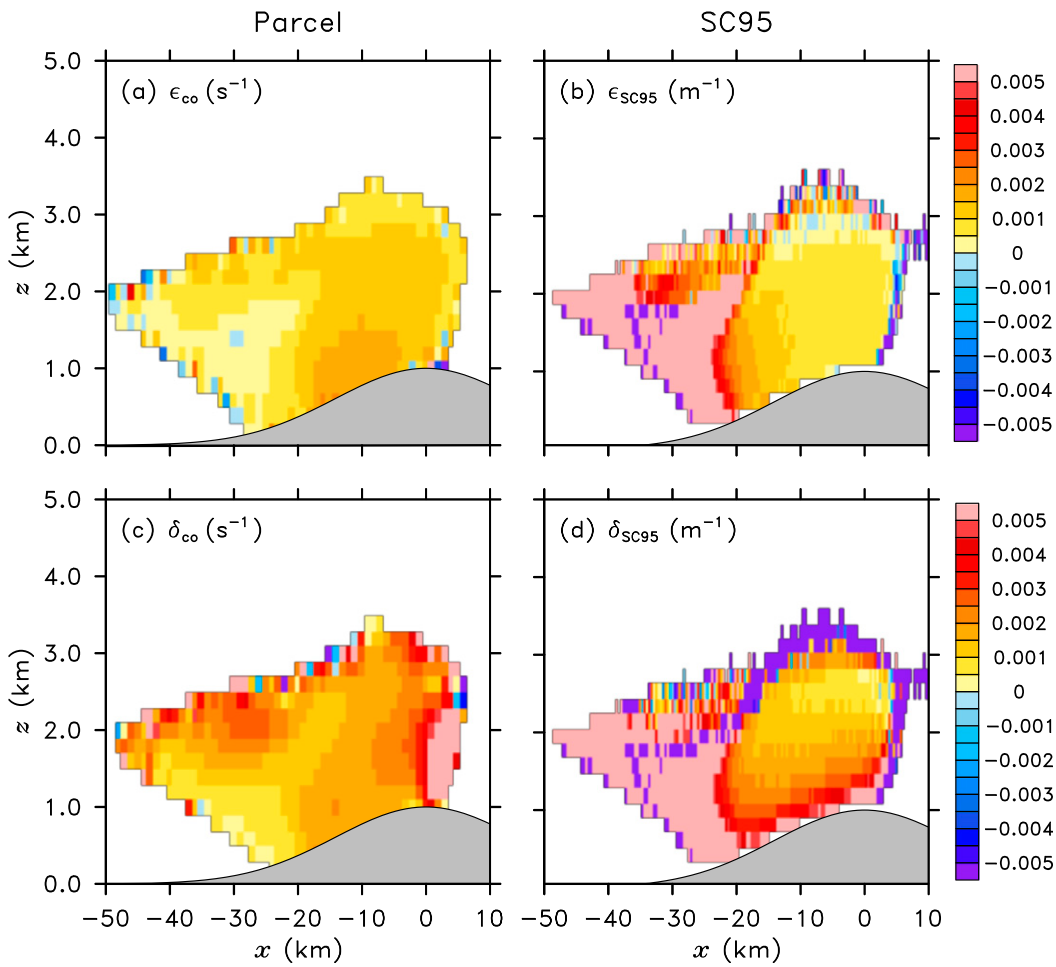

FIG. 6. (top) Entrainment and (bottom) detrainment calculations using (a),(c) the parcel-based method and (b),(d) the SC95 method, for the MECH-62m case. The units are s^{-1} in (a) and (c) and m^{-1} in (b) and (d).

facilitate comparison of the PAR and CP simulations, a bulk approach is taken.

SC95 derived a bulk Eulerian formulation of entrainment and detrainment in simulated cloud ensembles. They assumed that all clouds develop within the same environment, which is reasonable for horizontally homogeneous flows. However, this assumption breaks down in flows with large mesoscale variability, such as the orographic flows considered here. For example, the *y*-averaged environment in which incipient clouds develop differs strongly between the ridge base and crest. As clouds traverse the ridge, their environment continuously changes over their life cycle.

To overcome such challenges, we develop a new bulk entrainment/detrainment diagnosis that is suitable for cumuli in horizontally heterogeneous environments. As detailed in the appendix, this method relies on both parcel-trajectory and passive-tracer analyses to obtain 2D spatial fields of bulk entrainment ε_{co} and detrainment δ_{co}, both measured in units of s^{-1} (contrasting with the typical units of m^{-1}, as in SC95), where the "co" subscript refers to the buoyant cloud core. The advantage of this method is that entrainment and detrainment are inferred following the flow rather than within a vertical column, which accounts for horizontal and/or temporal environmental variability during cloud development.

To evaluate the performance of this method, we compare it to the corresponding SC95 formulation (denoted ε_{SC95} and δ_{SC95}) for the MECH-62m case in Fig. 6. For consistency, both methods are applied to cloud cores and use passive-tracer concentration as their conserved variable. Although SC95 was not designed for horizontally heterogeneous flows, it can be applied to them by averaging in the symmetric *y* dimension to obtain environmental profiles that vary in both *x* and *z*. Bulk entrainment and detrainment are then determined at each *x* location based on the local environmental profile and the conditionally *y*-averaged core properties.

Despite their differing units, the entrainment/detrainment magnitudes in the parcel method and SC95 are similar. This is because characteristic in-cloud vertical velocities in MECH are $W \sim O(1)$ m s^{-1}, and dividing by this near-unity factor retrieves the same units for both. However, the spatial structures of each quantity clearly differ. The parcel method gives a more sensible entrainment structure, with a relative minimum on the

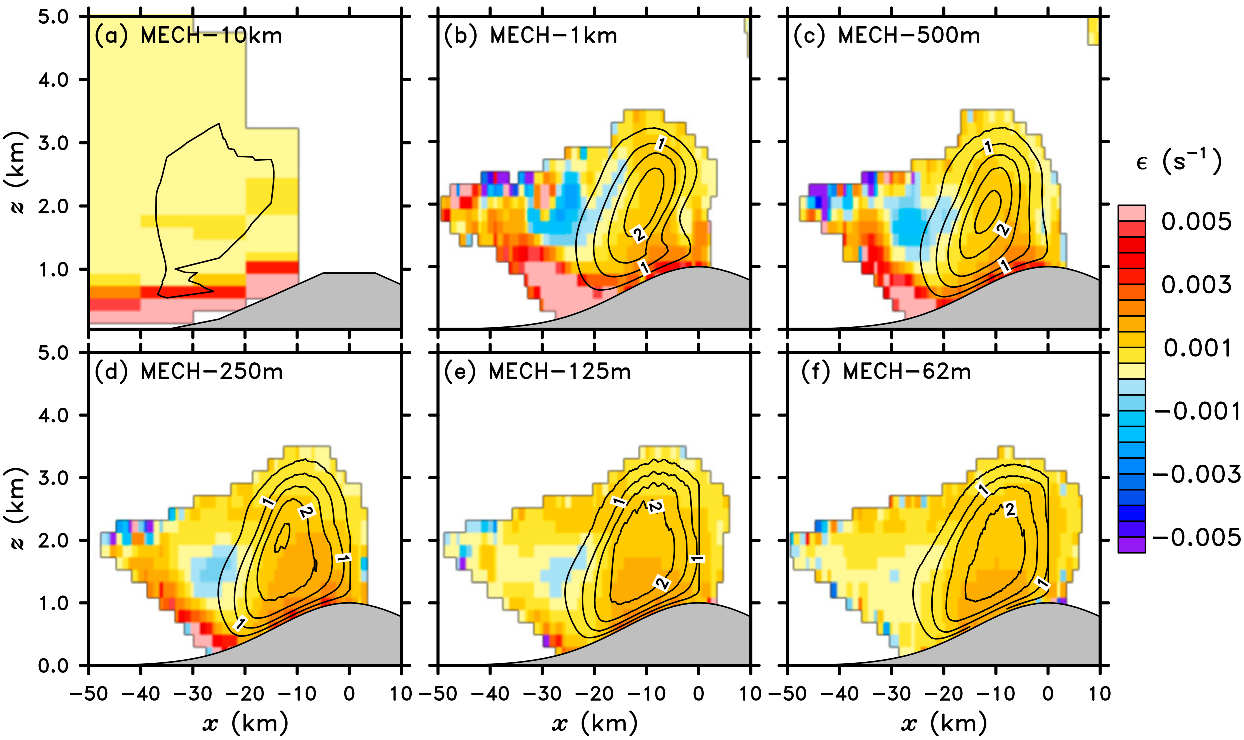

FIG. 7. Parcel-based entrainment rates for selected MECH simulations, averaged over all parcels traversing each grid box over the 3–6 h period. Core vertical mass flux M_{co} is also shown in black contours, in units of $10^4\,\mathrm{kg\,m^{-1}\,s^{-1}}$.

upwind side of the cloud and a maximum near the ridge crest, where local turbulence—and lateral mixing—is more intense (Fig. 6a). SC95, by contrast, gives nearly the opposite result (Fig. 6b), likely due to the assumption that all changes in conserved properties with height are owing to cloud dilution. This assumption is violated in MECH, where an entire layer of impinging flow is lifted to saturation en masse, and vertical profiles at the cloud leading edge resemble the environment itself. In SC95, such a profile would yield a massive entrainment rate. For detrainment, the parcel method again appears superior, with large detrainment in areas of strong evaporation near the cloud top and downwind edge. Counterintuitively, SC95 again gives large values at the leading edge and base of the cloud.

The parcel-based ε_{co} and δ_{co} for all the MECH simulations are shown in Figs. 7 and 8, overlaid by total (resolved plus subgrid) M_{co}, both averaged over 3–6 h. Although the cloud field at any instant consists of scattered cumuli distributed over the windward slope (Fig. 3), the time-averaged ε_{co} and δ_{co} are smooth due to the sampling of many parcels at differing locations and stages of development. In the parameterized MECH-10km case, ε_{co} is generally small except for a thin, surface-based layer of large values over the windward slope (Fig. 7a), and M_{co} is maximized above the mountain base at a height of 2 km. Much richer spatial variation in ε_{co} is found in the CP cases, and M_{co} shifts downstream and concentrates along a narrow, forward-tilting axis cutting through the cloud mass (Figs. 7b–f). Whereas large ε_{co} appears at both the cloud base and upstream edge in MECH-1km, these two maxima gradually weaken as Δ_h is decreased, leaving only a robust maximum over the downstream half of the cloud of around $2\times10^{-3}\,\mathrm{s}^{-1}$. At this rate, a parcel would become 50% diluted by environmental air in 8.3 min.

An area of negative ε_{co} centered at $x \approx -25$ km and $z \approx 1.5$ km appears in the CP cases and gradually vanishes as Δ_h is reduced (Figs. 7b–f). Counterintuitively, parcels traversing this area become *less* diluted by environmental air over time. In these bulk calculations, negative entrainment does not imply detrainment; each parcel is arbitrarily small and homogeneous, and thus detrainment cannot change its internal properties. Rather, we speculate that this patch of negativity stems from the local coincidence of weak turbulence (due to the laminar impinging flow) and elevated convection (due to an upstream-tilted mountain wave). As elevated cells initiate and traverse the ridge, their cloud bases descend toward the surface as the subcloud air approaches saturation. If vertical mixing between elevated core parcels and newly saturated parcels from below dominates over lateral mixing between the cores and their local environment, the elevated parcels would appear to become less dilute with time, thereby explaining the negative ε_{co}. The mitigation of this effect on the finer grids may be owing to stronger resolved turbulence, and hence an uptick in lateral mixing with the local environment.

As with ε_{co}, δ_{co} clearly differs between the PAR and CP runs. The parameterized δ_{co} in MECH-10km is generally weak over most of the orographic cloud except near cloud top

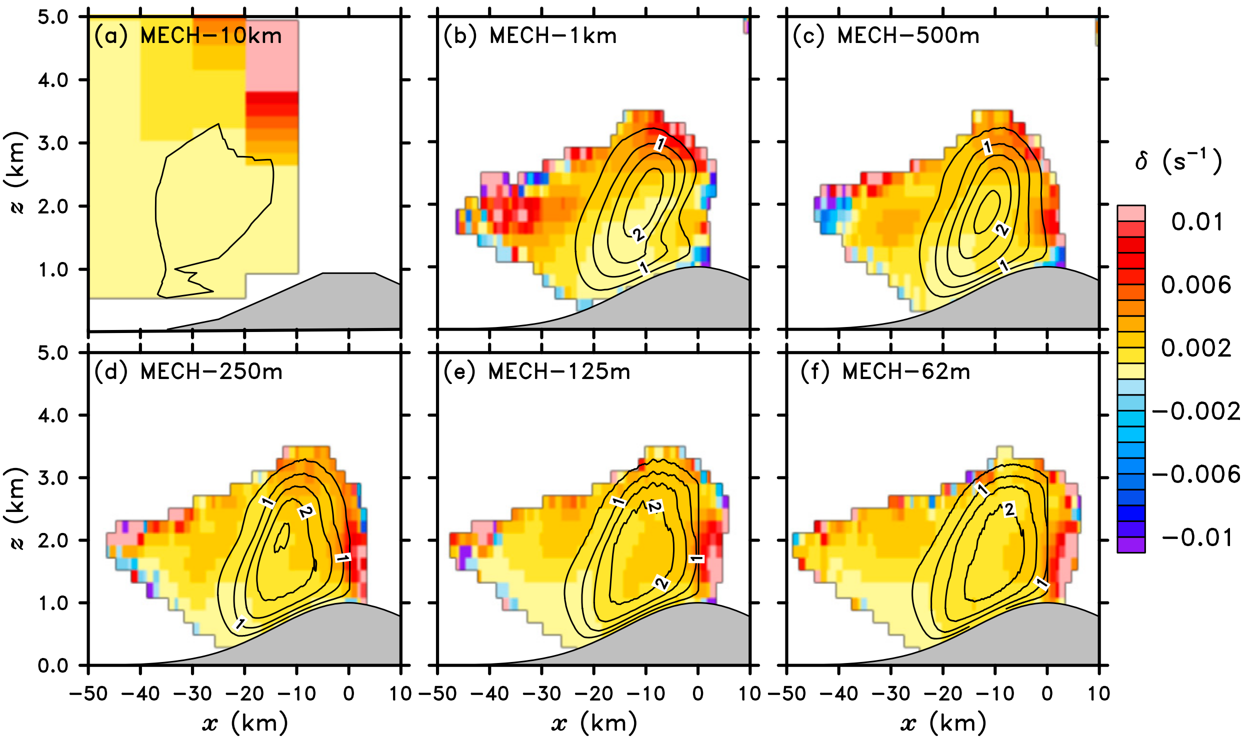

FIG. 8. As in Fig. 7, but for parcel detrainment.

(Fig. 8a). Detrainment is also relatively large near cloud top in the CP cases, but this maximum weakens—and detrainment in the cloud interior strengthens—as Δ_h is reduced (Figs. 8b–f). Thus, as Δ_h is decreased from $O(1)$ km to $O(100)$ m, the vertical entrainment and detrainment profiles transition from more bottom heavy (ε_{co}) and top heavy (δ_{co}) to more vertically uniform. Meanwhile, as δ_{co} gradually weakens near cloud top, it strengthens along the downstream cloud edge.

For a more quantitative evaluation of ε_{co} and δ_{co}, we take their M_{co}-weighted average in Fig. 9a. In the PAR cases, these averages are relatively small (0.5–$1 \times 10^{-3}\,\mathrm{s}^{-1}$), reflecting the generally weak corresponding values within the cloud interiors (Figs. 7a and 8a). Both quantities increase in the CP cases, with δ_{co} generally exceeding ε_{co}. As Δ_h is decreased, increasing ε_{co} and decreasing δ_{co} closes this gap, which favors increased M_{co} (Fig. 4b). No evidence of convergence in δ_{co}, or ε_{co} in particular, is found as Δ_h is decreased. Given that the magnitude of the Δ_h sensitivity exceeds the random variability within the 250-m ensemble, this trend appears to be significant.

The MECH-2km case represents a major outlier in the above comparison, with a pronounced increase in ε_{co} accompanied by a negative δ_{co} (the latter falling off the plot). The likely source of this unphysical behavior is the very marginal resolution of the shallow convective cells at $\Delta_h = 2$ km, which may give rise to substantial numerical errors at poorly resolved scales. Because this case fundamentally differs from the higher-resolution convection-permitting cases, we do not devote significant effort to understanding its errors. Rather, we simply emphasize that $\Delta_h = 2$ km is too coarse to represent the relatively shallow cumuli in these simulations.

c. *Structural convergence*

The CWP fields in Fig. 3 suggest a systematic decrease in cloud size as Δ_h is reduced. However, as Δ_h is decreased to 125 m and smaller, variations in mean cloud size become less obvious. To more quantitatively evaluate the sensitivity of cloud structure and vertical motion to Δ_h, the spectral density of resolved TKE (following Durran et al. 2017), averaged over 1.5–3 km and 3–6 h, along with histograms of cloud size and cloud-core size at 2 km and integrated over 3–6 h, are shown in Fig. 10. Herein, cloudy grid points are defined as those with total cloud mixing ratio (both liquid and ice cloud) exceeding $10^{-4}\,\mathrm{g\,kg}^{-1}$, and cloud-core grid points are additionally positively buoyant and ascending (relative to the local y average).

As the horizontal wavelength λ decreases from 10 km to 125 m (the smallest resolvable scale in MECH-62m), the slopes of the energy spectra generally transition from weakly negative to more strongly negative, with the transition scale depending on Δ_h (Fig. 10a). Except for MECH-62m and perhaps MECH-125m, none of these spectra have segments paralleling the $\kappa^{-5/3}$ line characteristic of 3D, isotropic turbulence. As Δ_h decreases, energy at the larger scales is increasingly removed by a stronger forward energy cascade. No convergence occurs on the microscale, where large Δ_h sensitivity persists down to MECH-62m. At scales of around $8\Delta_h$ and smaller, the spectra steepen due to implicit numerical diffusion (for $\Delta_h \leq 250$ m), suggesting an effective grid resolution of around $8\Delta_h$.

Like the microscale power spectra, histograms of effective cloud size D^c_{eff}, defined as the diameter of a cylindrical cloud of identical cross-sectional area as the measured one, do not converge to a robust distribution as Δ_h is decreased (Fig. 10b).

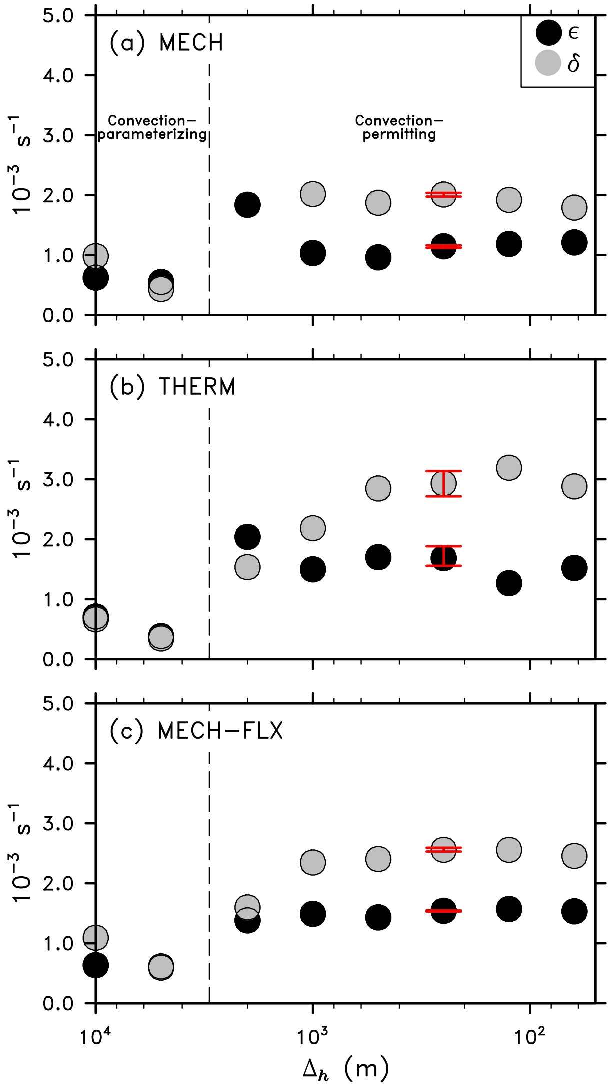

FIG. 9. Core-mass-flux-weighted entrainment and detrainment for the (a) MECH simulations over 3–6 h, (b) THERM simulations over 1–3 h, and (c) MECH-FLX simulations over 3–6 h. The range of values in the 250-m ensemble is indicated by red error bars.

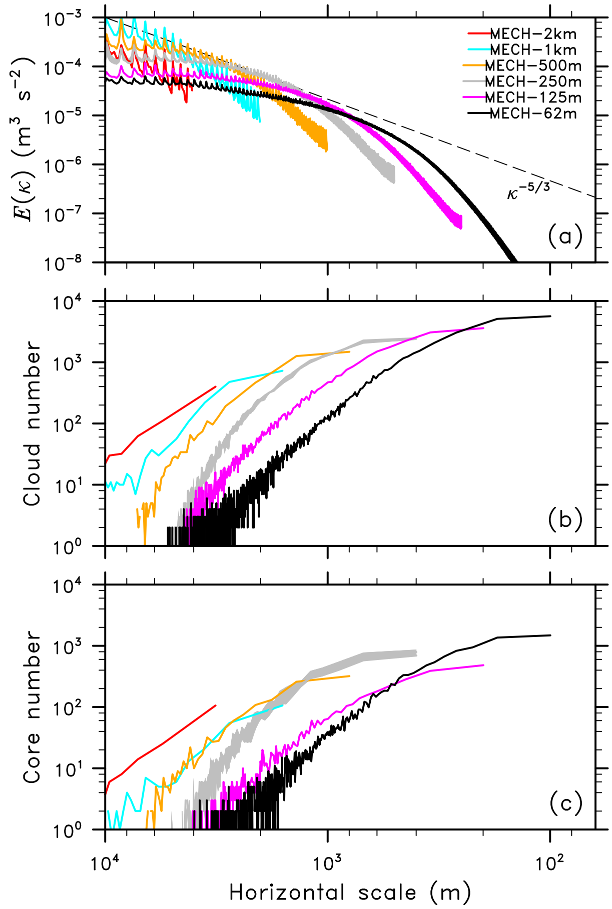

FIG. 10. Variation of structural properties among the CP MECH simulations. (a) Two-dimensional energy spectral density, averaged in height over 1.5–3 km and in time over 3–6 h, (b) cloud-size number distribution, and (c) core-size number distribution, both evaluated at a height of 2 km and in time over 3–6 h. The horizontal scale on the abscissa refers to wavelength in (a), cloud diameter in (b), and core diameter in (c). The gray-shaded area for the MECH-250m case indicates the range of values in the corresponding five-member ensemble.

The peaks of these distributions robustly fall at the smallest allowable size bin Δ_h and decrease similarly with increasing D^c_{eff}. Histograms of effective cloud-core size $D^{\mathrm{co}}_{\mathrm{eff}}$ also show a systematic decrease in core number with increasing $D^{\mathrm{co}}_{\mathrm{eff}}$, and progressively shift toward smaller sizes as Δ_h is decreased (Fig. 10c).

4. Thermal forcing

Snapshots of CWP at 3 h of the THERM CP cases indicate generally larger CWP and cloud fraction at larger Δ_h, with arguably the strongest convection in THERM-1km (Fig. 11). The trend for cloud fraction to decrease with decreasing Δ_h holds down to $\Delta_h = 250$ m, beyond which further variations in CWP are modest. The low-level inflow is also the strongest in THERM-1km, becoming weaker and more variable at smaller Δ_h.

a. *Bulk convergence*

The PAR cases initiate DMC well before the CP cases (around 1.5 versus 3 h; Fig. 12a). This early onset of DMC is consistent with the diurnal phase errors in most cumulus schemes (e.g., Dai 2006; Dirmeyer et al. 2012; Stirling and Stratton 2012). Similarly, convective mass flux and precipitation develop 1–2 h too early in the PAR cases. While the mass fluxes reach comparable levels to the CP cases later in the model integration, the peak instantaneous precipitation rates only reach about half of those in the CP cases (Figs. 12b,c). Such underprediction of precipitation intensity is another well-known bias of cumulus schemes (e.g., Dai 2006).

Among the CP cases, increasing grid resolution generally delays convection initiation and weakens the peak convective mass fluxes (Fig. 12). A period of shallow convection, characterized by 2–3-km cloud tops, dominates from 1 to 2.5 h, followed

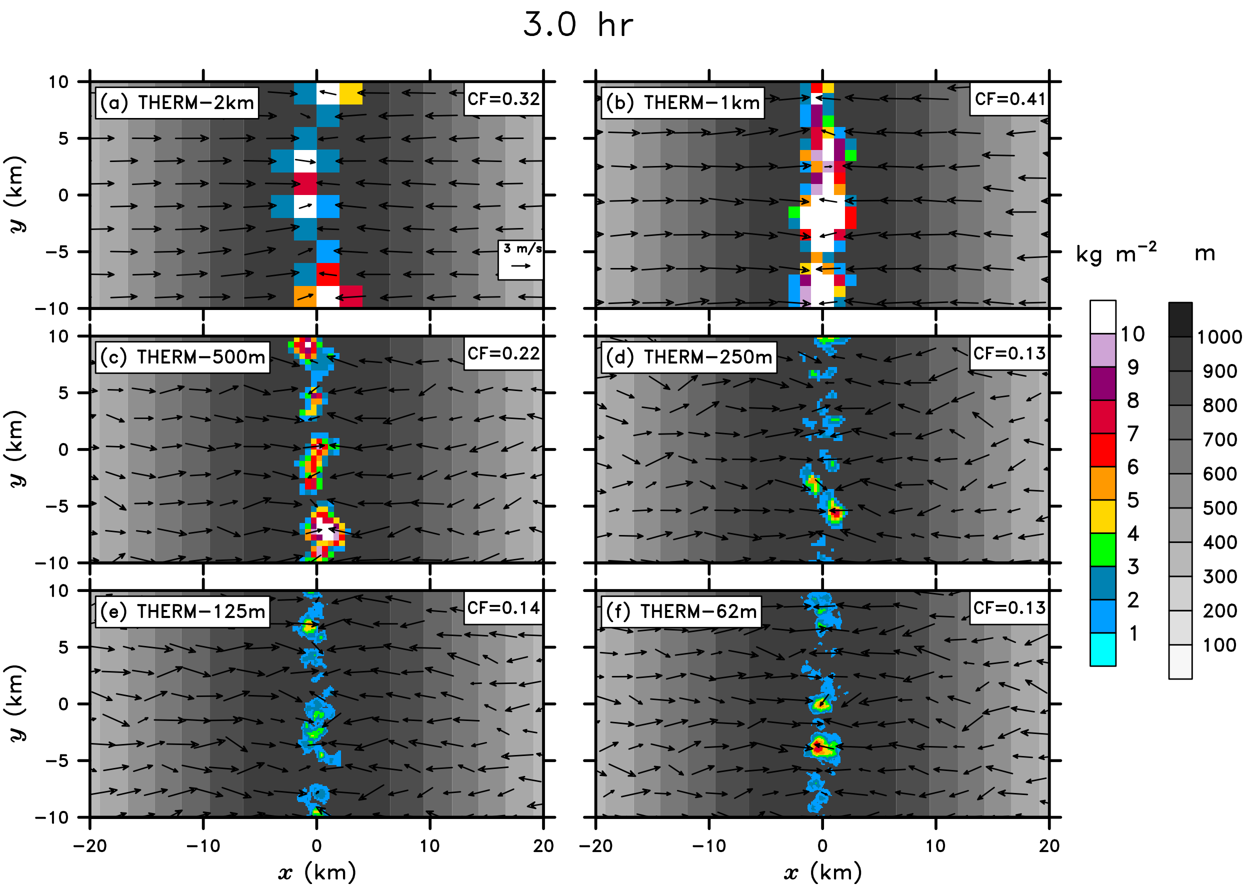

FIG. 11. As in Fig. 3 but for the THERM simulations. The cloud fraction (CF) is calculated over $|x| \le 5$ km.

by a rapid transition to much deeper, precipitating convection with cloud tops exceeding 15 km (2.5–3.5 h). The timing of this transition varies with Δ_h, with the earliest transition in THERM-1km (centered at 2.6 h) and the latest transition in THERM-62m (centered at 3.2 h). However, the differences for $\Delta_h \le 250$ m are comparable to the random variability of the 250-m ensemble, suggesting numerical convergence at those scales. The onset of bulk convergence and robustness are thus estimated as Δ_h = 1 km and Δ_h = 250 m, respectively.

The 40-min difference in the timing of convection initiation across the CP cases is less dramatic than that found in Tang and Kirshbaum (2020), where Δ_h regulated cloud-top heights over the entire diurnal cycle. However, these differences are still noteworthy because even a small error in the timing of convection initiation can significantly impact the larger-scale flow, particularly through resulting errors in precipitation and radiation. Given that global climate models are highly sensitive to details of cumulus representation (e.g., Rougier et al. 2009), such errors could lead to significant biases in climate projections.

Along with developing convection too early, the PAR cases spread precipitation too widely over the ridge, with an accompanying reduction in intensity (Fig. 5b). In the CP cases, a much narrower distribution centered over the crest narrows further and reaches larger peak values as Δ_h is decreased. As in the MECH experiments, convergence of the spatial precipitation distribution is more elusive than that of total precipitation, with the onset of bulk convergence at Δ_h = 500 m (where a monotonically increasing trend in the maximum R begins) and robustness at Δ_h = 125 m (where further changes with decreasing Δ_h are negligible).

b. Entrainment and detrainment

Parcel-based ε_{co} and δ_{co} for selected THERM cases are shown in Figs. 13 and 14, with the core-mass-flux-weighted ε_{co} and δ_{co} shown in Fig. 9b. This analysis is conducted over 1–3 h, where subcloud turbulence is established but the cloud depth depends strongly on Δ_h (Fig. 15a). In general, δ_{co} is smaller on the coarser grids (Figs. 14 and 9b), which promotes deeper convection. As Δ_h is decreased, δ_{co} increases to a plateau at Δ_h = 500 m, favoring a more rapid cloud dissipation with height. By contrast, ε_{co} has much less influence on cloud-top height: it is again the smallest in the PAR cases, increases sharply to a maximum in THERM-2km, and then remains nearly constant. Despite this near-convergence of ε_{co} for $\Delta_h \lesssim 1$ km, the cloud-top height still progressively decreases as Δ_h is further reduced (Figs. 13c–f).

Structurally, ε_{co} tends to decay strongly with height in both the THERM-10km and THERM-1km cases (Figs. 13a,b), as

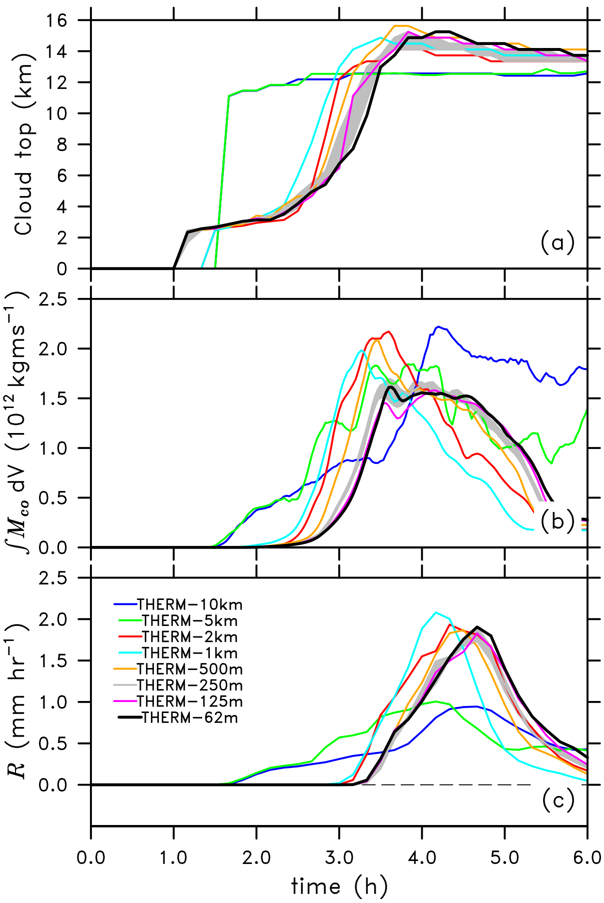

FIG. 12. As in Fig. 4, but for the THERM simulations.

well as in THERM-5km and THERM-2km (not shown). However, this decay largely vanishes for $\Delta_h \leq 500$ m (Figs. 13c–f), which likely stems from changes in cloud mixing processes as grid-resolved turbulence increases. In contrast, δ_{co} transitions from a cloud-top maximum in PAR cases to maxima along the lateral cloud edges in CP cases. Thus, both ε_{co} and δ_{co} become more horizontally variable but vertically uniform as Δ_h is decreased.

In the MECH simulations, an organized area of negative ε_{co} was found in the cloud overhang region (Fig. 7). In the associated discussion, we speculated that this nonintuitive behavior was associated with elevated convection mixing vertically with underlying air as it roots to the surface. This notion is supported by the THERM simulations, where all clouds are surface-based (rather than elevated) upon initiation and thus already rooted to the surface. As a result, no organized areas of $\varepsilon_{co} < 0$ are found. The isolated pixels with $\varepsilon_{co} < 0$ are mostly scattered around the cloud periphery, in poorly sampled areas traversed by very few core parcels over the model integration.

The M_{co}-weighted ε_{co} and δ_{co} again indicate very weak environmental mixing in the PAR cases, which promotes an early onset of DMC (Fig. 9b). Among the CP cases, ε_{co} and δ_{co} become statistically similar for $\Delta_h \leq 500$ m. Although fluctuations in these quantities continue to occur down to the smallest Δ_h, the differences are similar in magnitude to the random variability of the 250-m ensemble. Thus, as in Fig. 12, the onset of numerical convergence and robustness in ε_{co} and δ_{co} are roughly achieved at $\Delta_h = 1$ km and 250 m, respectively.

c. *Structural convergence*

Qualitatively, the cloud sizes appear to decrease with decreasing Δ_h in the THERM simulations, at least for grid spacings down to $\Delta_h = 250$ m (Fig. 11). A similar trend is suggested by TKE spectral density at midlevels (2.5–4 km), the magnitude of which progressively decreases in the mesoscale ($\lambda = 10$–2 km) for $\Delta_h > 125$ m (Fig. 15a). On the microscale, a larger portion of the spectrum parallels the $\kappa^{-5/3}$ line for $\Delta_h \leq 250$ m than in the corresponding MECH cases, reflecting a mature turbulence field owing to the underlying convective PBL. The main differences in the spectra for $\Delta_h \leq 250$ m stem from numerical diffusion at scales of around $8\Delta_h$ and less. Notwithstanding such discrepancies near the grid scale, these spectra achieve robustness at $\Delta_h \approx 125$ m.

Numerical convergence is not achieved in the D^c_{eff} or D^{co}_{eff} spectra, which are analyzed at a height of 3 km over 2–4 h (Figs. 15b,c). As Δ_h is decreased, the clouds and cores again systematically shift toward smaller sizes, and the marginal changes between the simulations are maintained. Thus, although bulk quantities and power spectra of the THERM simulations are more convergent than those in the MECH simulations, the cloud and core sizes still fail to converge in both cases.

d. *Subcloud forcing*

Although the analysis thus far has focused on the sensitivity of cloud-layer processes to Δ_h, notable differences in subcloud (i.e., PBL) properties also exist (e.g., Fig. 2) and should be taken into consideration. The numerical representation of subcloud processes, including turbulent eddies and organized subcloud updrafts, may vary widely within the turbulence gray zone. Recent studies have found that such variations may strongly regulate moist convection within the overlying cloud layer (e.g., Rousseau-Rizzi et al. 2017; Tang and Kirshbaum 2020).

Vertical cross sections of w and mean-layer LFC height, averaged in y and in time over part of the preconvective period (1.5–2.5 h), are shown for the THERM CP runs in Fig. 16. In all cases, a strong thermally forced updraft is centered at $x = 0$ km, surrounded by ascending, terrain-parallel inflow at lower levels and descending outflow aloft. As Δ_h is decreased, the updraft core gradually weakens and the LFC rises. Both of these trends stem from increased total turbulence [resolved plus subgrid, where the former is $\mathrm{TKE}_{res} = \rho/2(u'^2 + v'^2 + w'^2)$] in the subcloud layer (Fig. 17a). The associated enhancement in lateral mixing tends to widen and weaken the updraft (as in Tang and Kirshbaum 2020), and the enhanced vertical mixing brings more free-tropospheric air into the PBL to locally decrease q_v (Fig. 17b) and raise the LFC (as in Panosetti et al. 2016). This latter trend reverses away from the mountain crest, where the PBL top lies below 500 m AGL. These sensitivities to Δ_h hold down to $\Delta_h = 250$ m and then largely abate.

The combined effect of a weaker subcloud updraft and a higher LFC yields a progressive reduction in core-base M_{co}

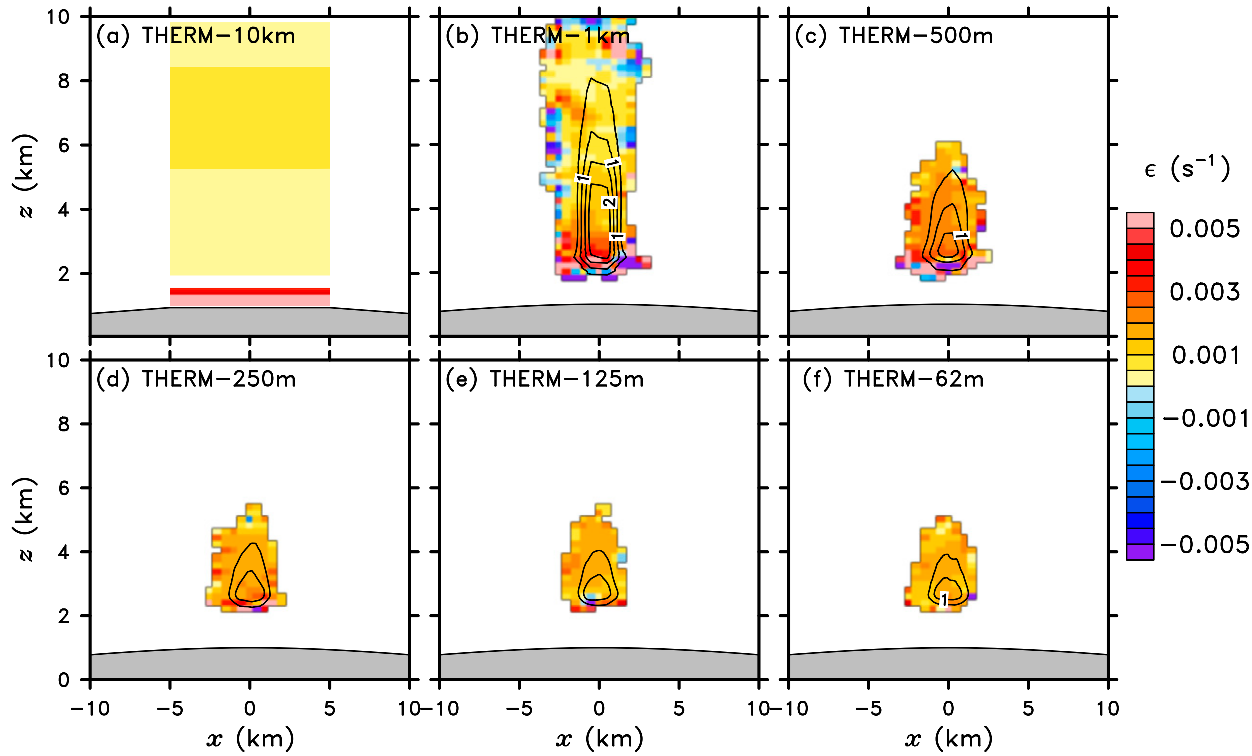

FIG. 13. As in Fig. 7, but for the THERM simulations over 1–3 h.

(or M_{cb}) with decreasing Δ_h over 2–3.5 h (Fig. 18). In particular, M_{cb} is substantially larger in THERM-2km and THERM-1km than in THERM-125m and THERM-62m. To isolate the effects of increased LFC height versus reduced updraft strength on this trend, we recompute M_{cb} for THERM-62m using the LFC taken from the THERM-1km case (and interpolated to the 62-m grid). As shown by the dashed line in Fig. 18, the higher LFC explains about half of the increase in M_{cb} in THERM-1km, relative to the

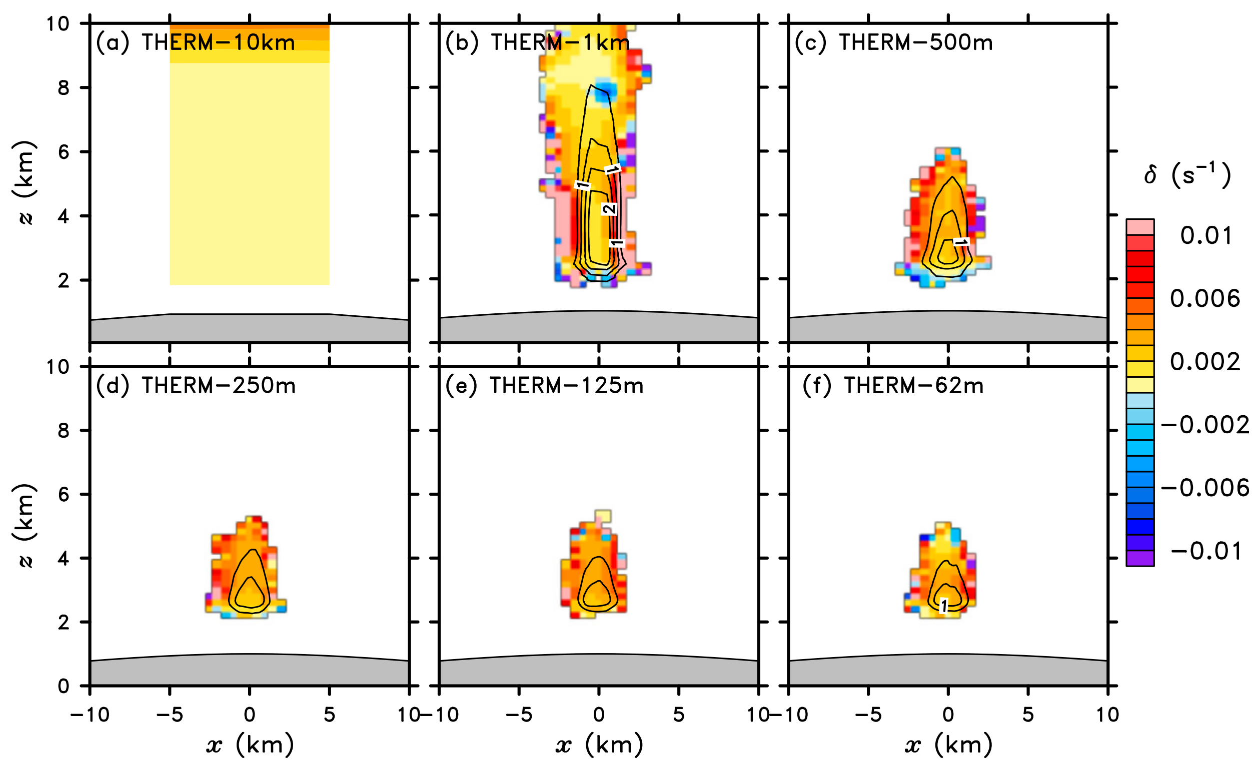

FIG. 14. As in Fig. 8, but for the THERM simulations over 1–3 h.

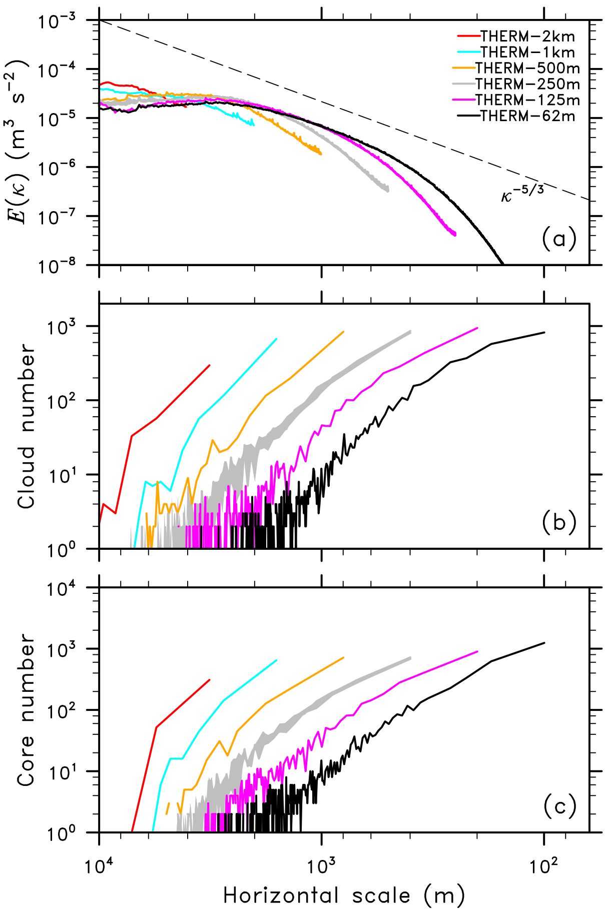

FIG. 15. Variation of structural properties among the CP THERM simulations. (a) Two-dimensional energy spectral density, averaged in height over 2.5–4 km and in time over 1–3 h, (b) cloud-size number distribution and (c) core-size number distribution, both evaluated at a height of 3 km and in time over 2–4 h. The horizontal scale on the abscissa refers to wavelength in (a), cloud diameter in (b), and core diameter in (c). The gray-shaded area for the THERM-250m case indicates the range of values in the corresponding five-member ensemble.

reference THERM-62m case. The remainder may thus be attributed to the more diffuse subcloud updraft at smaller Δ_h.

The trend for M_{cb} to strengthen with increasing Δ_h over 2–3.5 h in Fig. 18 is consistent with the trend in volume-integrated M_{co} in Fig. 12b, but weaker in magnitude. At 2.5 h, for example, the volume-integrated M_{co} in THERM-1km is about 4 times that of THERM-62m (Fig. 12b), while the corresponding M_{cb} is only about twice as large. Thus, subcloud processes appear to only explain about half of the increase in M_{co} with increasing Δ_h.

5. Discussion

a. Subcloud versus cloud-layer mass fluxes in THERM

Within the cloud layer, the controls on convective mass flux may be roughly interpreted using a simple expression for M_{co} derived from Betts (1975):

$$M_{co} = M_{cb} \exp\left[\int_{LFC}^{z} (\varepsilon_{co} - \delta_{co})\, dz\right]. \quad (1)$$

In this formulation, M_{co} depends linearly on cloud-base mass flux M_{cb}, which is largely regulated by subcloud processes, and exponentially on cloud-layer mixing processes (ε_{co} and δ_{co}). Evaluating (1) by substituting M_{cb} at 2.5 h (Fig. 18) and ε_{co} and δ_{co} (Fig. 9b), the resulting vertically integrated M_{co} is estimated to be 3.7 times larger in THERM-1km than in THERM-62m, consistent with the corresponding differences over 2–3 h in Fig. 12b. Given that about half of the decrease of volume-integrated M_{co} over 2–3 h in the higher-resolution simulations was explained by subcloud processes (section 4d), the remainder is owing to the more negative cloud-layer $\varepsilon_{co} - \delta_{co}$.

The above analysis facilitates an estimation of the impacts of eschewing a PBL parameterization in the THERM simulations. As just discussed, subcloud processes account for only about half of the Δ_h sensitivity in Fig. 12b, so part of this sensitivity would likely persist even if the PBL growth was independent of Δ_h. Also, because many PBL schemes (including the 1D version of Hong et al. 2006) only parameterize vertical mixing, they could not reproduce the lateral-mixing-induced widening and weakening of the subcloud updraft at $\Delta_h \le$ 250 m. This latter effect accounts for about half of the sensitivity of M_{co} to subcloud processes (see section 4d), so variations in PBL depth alone must only account for around 25% of the Δ_h sensitivity in the THERM experiments.

b. Comparing the MECH and THERM experiments

In the MECH experiments, only partial bulk convergence and no structural convergence was found as Δ_h was systematically decreased. The spatial precipitation distribution, power spectrum, cloud/core size distributions, and entrainment and detrainment exhibited little if any signs of convergence. In contrast, the THERM cases exhibited full convergence of these same metrics (except for the cloud/core sizes) for $\Delta_h \le$ 125 m, suggesting that this configuration is less sensitive to Δ_h. In this section, we attempt to physically explain these contrasting sensitivities.

We hypothesize that two key factors differentiate the MECH and THERM simulations. First, the flow brought to saturation over the ridge is initially laminar in MECH (due to the absence of a PBL) but turbulent in THERM. As a result, the former undergoes a transition to turbulence as it traverses the ridge while the latter does not. The dynamics of this transition depends on Δ_h, as finer grids support sharper gradients in wind and thermodynamic fields and can resolve fast-growing microscale instabilities. As a result, the kinetic energy spectrum (Fig. 10a) and the dynamics of mixing between the clouds and their surroundings also depend on Δ_h.

In contrast, thermals originating in the subcloud layer of the THERM simulations are already turbulent upon breaching the LFC, with a well-developed inertial subrange for $\Delta_h \le$ 250 m (Fig. 15a). Moreover, given that subgrid turbulence schemes generally assume that Δ_h lies well within the inertial subrange (e.g., Leonard 1975; Bryan et al. 2003), these schemes should exhibit superior performance in the THERM cases, at least for $\Delta_h \le$ 250 m. The scale awareness of the Deardorff (1980)

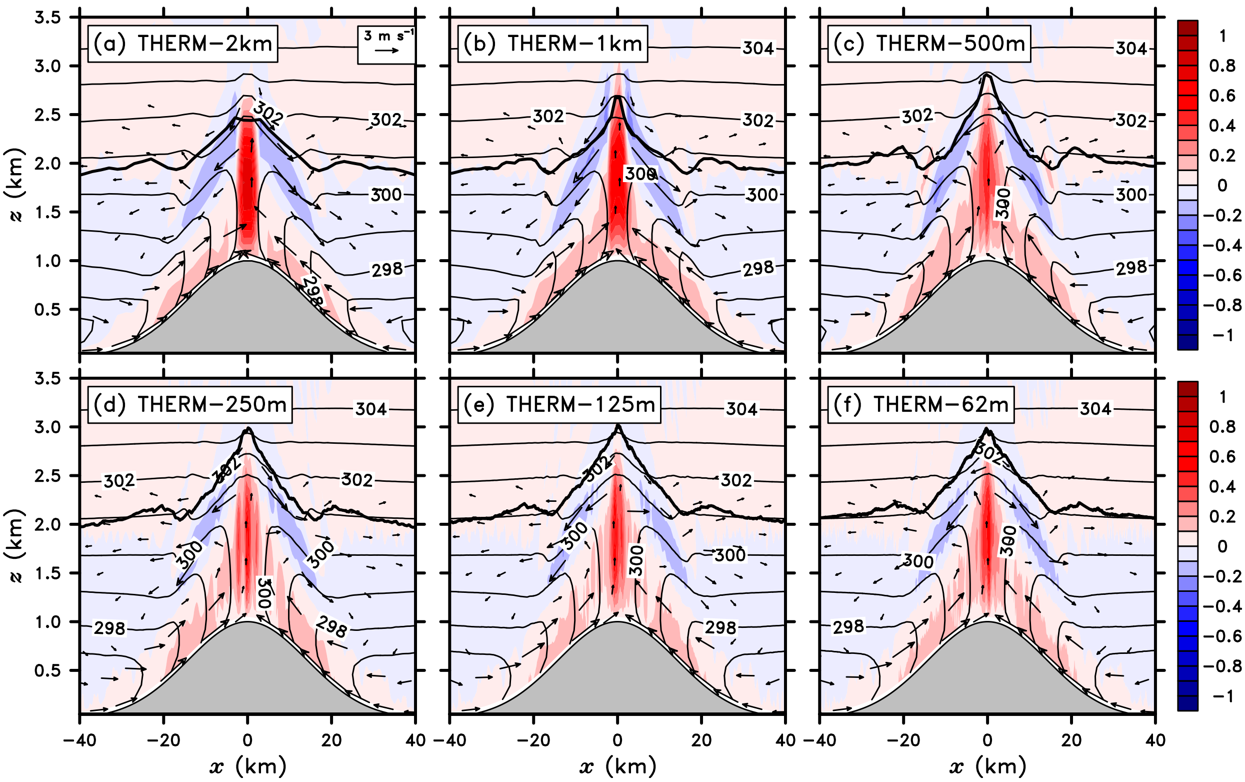

FIG. 16. Time- and y-averaged vertical cross sections of w (color fill; m s^{-1}), potential temperature θ (black contours; intervals of 1 K), plane-parallel wind vectors, and mean-layer LFC (thick black line) over 1.5–2.5 h, for selected THERM simulations.

scheme allows the THERM simulations to maintain a nearly constant total turbulence magnitude as Δ_h is reduced below 250 m (Fig. 17a).

The above hypothesis can be critically evaluated by either (i) enhancing the upstream turbulence in the MECH experiments or (ii) reducing the subcloud turbulence in the THERM experiments. For practical reasons we choose the first option, which can be achieved in various ways. Although adding corrugation to the terrain constitutes one such method (e.g., Miglietta and Rotunno 2009), we prefer to keep the terrain unchanged for consistency across all experiments. We therefore add a strip of heated land upstream of the ridge, with a sensible heat flux of 50 W m^{-2} over $x \in [-120, -60]$ km. This surface heating generates a turbulent and well-mixed PBL extending up to around 400 m AGL (not shown), which is subsequently lifted to saturation over the ridge. This set of simulations is termed ''MECH-FLX.''

As indicated by 1D TKE spectra in y at different zonal locations within the orographic cloud (Fig. 19), upstream surface heating expedites the development of cloud-layer turbulence. In mature turbulence fields in LES, such spectra tend to exhibit increased power with decreasing scale until reaching kink in the mesoscale, thereafter following a $\kappa^{-5/3}$ slope through the inertial subrange (e.g., Fig. 15a). Although this shape does ultimately develop in MECH, it is limited to a small region near the crest ($x \geq -10$ km; Figs. 19a,b). By contrast, it prevails through most of the orographic cloud in MECH-FLX (Figs. 19c,d). Moreover, the sensitivity of the spectra to Δ_h is stronger in MECH than in MECH-FLX, particularly near the upstream end of the orographic cloud ($x < -20$ km). As Δ_h is reduced, a microscale peak strengthens and shifts to smaller scales in MECH, indicating substantial dynamical variability between even the highest-resolution cases. This feature is highly subdued in MECH-FLX.

Comparison of bulk and structural properties between the MECH and MECH-FLX simulations supports the notion that the presence of resolved turbulence weakens the sensitivity to Δ_h within the turbulence gray zone. The robustness scale for volume-integrated M_{co} appears to increase from $\Delta_h = 125$ m in MECH to $\Delta_h = 250$ m in MECH-FLX (Figs. 4b and 20). In addition, the rainfall distribution is less sensitive to Δ_h in MECH-FLX than in MECH, where it underwent major positional shifts even for $\Delta_h \leq 250$ m (cf. Figs. 5a and 5c). Finally, and most strikingly, in contrast to the MECH experiments where ε_{co} and δ_{co} did not numerically converge, these quantities converge to robust values at $\Delta_h \approx 500$ m in MECH-FLX (cf. Figs. 9a and 9c).

The flattening of the precipitation distribution in MECH-FLX (relative to MECH; Figs. 5a,c) follows from two factors. First, on the upstream side of the crest, stronger vertical-velocity perturbations in the impinging flow of MECH-FLX induce saturation farther upstream of the crest. Second, on the downstream side, the more upright structure of the mountain wave shifts the locus of strongest convection toward the crest,

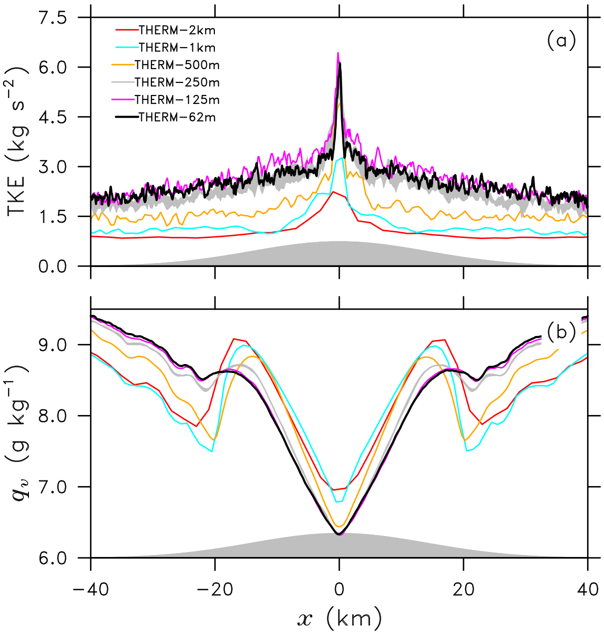

FIG. 17. Horizontal profiles of time- (over 1.5–2.5 h) and y-averaged (a) total (resolved plus subgrid) TKE and (b) q_v for the convection-permitting THERM cases at 500 m AGL. Scaled terrain is shown on each panel for reference. The gray-shaded area for the THERM-250m case indicates the range of values in the corresponding five-member ensemble.

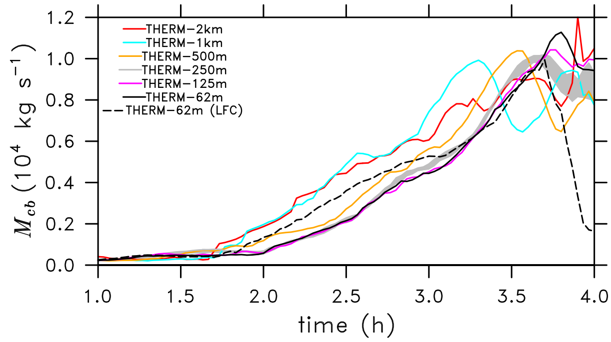

FIG. 18. Time series of core-base (LFC) upward mass flux M_{cb}, integrated over $|x| \leq 20$ km, for the convection-permitting THERM cases. The dashed curve named THERM-62m (LFC) indicates the M_{cb} in the THERM-62m case if the LFC was set to that in the THERM-1km case. The gray-shaded area for the THERM-250m case indicates the range of values in the corresponding five-member ensemble.

which decreases the windward-slope precipitation but enhances the spillover into the lee. This change in mountain-wave structure arises from the upstream heating, which reduces the static stability and thereby increases the vertical wavelength (e.g., Durran 1990).

The second factor differentiating MECH and THERM is the presence of mean ascending motion within the cloud layer in MECH. As incipient clouds develop, they benefit from this "background" terrain-forced ascent, which reinforces the positive buoyancy within the cloud cores (Kirshbaum and Smith 2009). As a consequence, cloudy parcels are less inclined to become negatively buoyant and detrain. This factor is evident in Fig. 9, where, for $\Delta_h \leq 500$ m, δ_{co} is generally larger in THERM (0.003 s^{-1}) than in MECH (0.002 s^{-1}) or MECH-FLX (0.0025 s^{-1}).

6. Conclusions

This study has quantified and interpreted the sensitivity of simulated orographic convection to horizontal grid spacing Δ_h across the deep-convection ($\Delta_h \sim$ from 10 km down to 1 km) and turbulence ($\Delta_h \sim$ from 1 km down to 62.5 m) gray zones. The simulations were idealized, with a smooth and y-periodic 1D mountain ridge focusing the convection, to help isolate and quantify the processes underlying the sensitivities to Δ_h. Two different mechanisms of terrain-forced ascent were simulated: mechanically forced convection as impinging flow was forcibly lifted to saturation by the ridge (MECH), and thermally forced convection as quiescent flow was heated at the surface (THERM). The latter generated a convective PBL and a mountain thermal circulation that lifted subcloud air to saturation.

Over the deep-convection gray zone, parameterized convection (with the widely used Kain–Fritsch cumulus scheme, for $\Delta_h \geq 5$ km) transitioned to explicit convection. The sensitivities to Δ_h were dominated by errors in the cumulus scheme, with convection forming too far upstream of the terrain in MECH and deep convection initiating too early in THERM. The MECH errors were consistent with the windward-lee effect (e.g., Schwitalla et al. 2008), where too much convective precipitation falls over the windward slope and too little falls over the lee. The THERM errors were consistent with the tendency for parameterized convection to initiate too early in the diurnal cycle (e.g., Dirmeyer et al. 2012).

Over the turbulence gray zone, the behavior of the MECH and THERM experiments fundamentally differed. Whereas the convective mass flux and precipitation in MECH tended to increase as Δ_h was reduced, it did the opposite in THERM (prior to the initiation of deep convection). These differences were partially attributed to the model representation of cloud entrainment and detrainment, which was diagnosed using a new parcel-based bulk method appropriate for horizontally heterogeneous flows. In MECH, entrainment increased and detrainment decreased as Δ_h was decreased, leading to increased convective mass fluxes. In THERM, by contrast, detrainment exhibited the dominant sensitivity to Δ_h, increasing with decreasing Δ_h to yield reduced convective mass fluxes. This latter behavior is consistent with the findings of Tang and Kirshbaum (2020) for simulated convection over a thermally forced convergence line.

Numerical convergence was assessed based on the Δ_h sensitivities of various bulk (cloud-ensemble mean or maximum) and structural (horizontal-scale-related) quantities (Panosetti et al. 2019). While some bulk properties of the MECH simulations, including cloud-top height, convective mass flux, and cumulative precipitation, converged, other bulk properties, including rainfall distribution, entrainment, and detrainment,

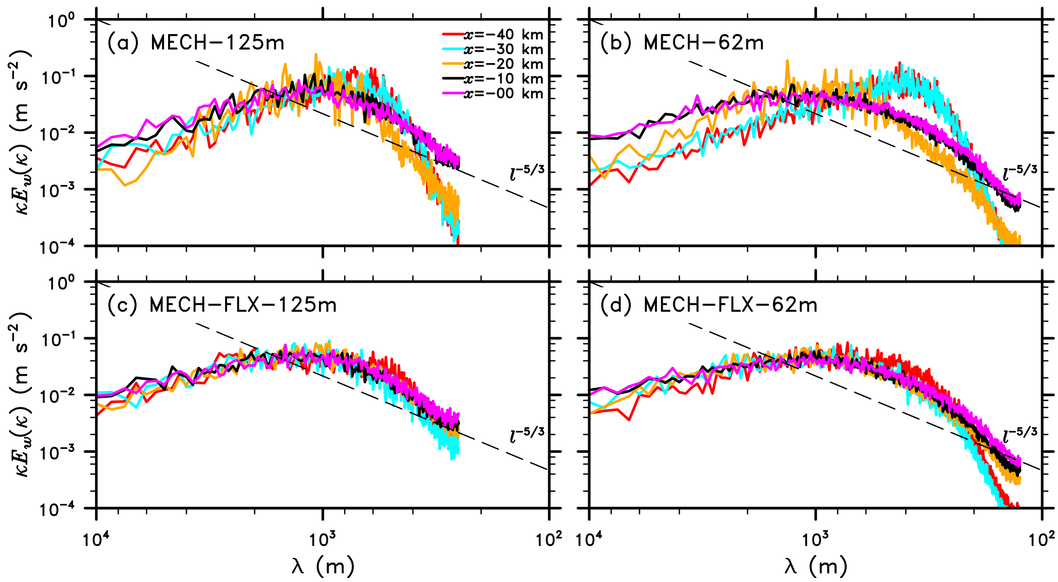

FIG. 19. One-dimensional (in y) energy spectral densities of selected simulations at a height of 2 km and five different zonal locations across the orographic cloud. All spectra are averaged in time over 3–6 h and, for ease of viewing, are normalized by the corresponding vertical-velocity variance. The dashed line indicates the $l^{-5/3}$ spectral slope, where l is the y wavenumber.

did not. Moreover, none of the structural properties (energy spectra, cloud/core size distributions) converged either. The THERM simulations, by contrast, were generally more convergent, with full bulk convergence and partial structural convergence for $\Delta_h \leq 125$ m (in power spectra but not cloud/core sizes).

Within the turbulence gray zone, differences in numerical convergence between MECH and THERM were attributed to the presence (or lack thereof) or resolved turbulence on the model grid. Although the higher-resolution MECH cases used appropriate values of Δ_h for large-eddy simulation, the flow impinging on the terrain was initially laminar due to the absence of a simulated PBL. A transition to turbulence occurred only as moist instabilities developed over the ridge. The speed of this transition depended on both zonal location and Δ_h, and the transition was not complete until the flow nearly reached the crest. Note that, had these flows been characterized by stronger moist instability, as in the MECH-like simulations of Miglietta and Rotunno (2012), this transition would likely have been hastened. In contrast, surface heating in THERM gave rise to a fully turbulent PBL, from which thermals penetrated into the cloud layer. The absence of a turbulent transition, and its attendant Δ_h dependence, as well as the development of an explicit inertial subrange for $\Delta_h \leq 250$ m (a basic assumption of the chosen subgrid turbulence closure), rendered the THERM simulations much less sensitive to Δ_h.

These findings highlight that, like moist convection over flat terrain, orographic convection is challenging to represent within both the deep-convection and turbulence gray zones. In the former, a common cumulus parameterization failed to adequately represent the timing and spatial distribution of orographic convection. Alleviation of such errors requires improved and more scale-aware cumulus schemes, which is a topic of intensive research (e.g., Bechtold et al. 2014). Within the turbulence gray zone, errors in cloud-base mass flux and cloud-layer entrainment and detrainment were found at coarser grid spacings [$\Delta_h \sim O(1)$ km], mainly owing to an inability of the subgrid turbulence closure to compensate for a lack of resolved turbulent mixing. Improvements to these schemes, such as accounting for interactions between subgrid and resolved motions (e.g., Moeng et al. 2010; Shi et al. 2019a) and accounting for the degree of turbulence on the resolved grid, are needed. Moreover, while our use of a smooth mountain ridge in these experiments was a useful simplification, more realistic and rugged terrain should be considered in future work. Last but not least, the sensitivity to other physical factors including aerosol loading, mountain geometry, thermodynamic conditions, and winds, and surface forcing merit further examination.

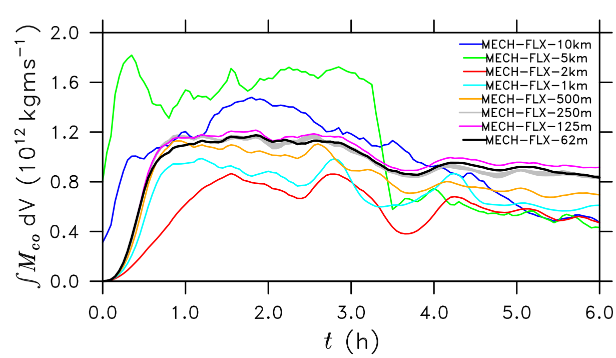

FIG. 20. As in Fig. 4b, but for the MECH-FLX simulations.

Acknowledgments. This research was supported in part by the U.S. Department of Energy's Atmospheric System Research, an Office of Science Biological and Environmental Research program, under Grant DE-SC0020083, as well as by the Natural Science and Engineering Research Council (NSERC) under Grant NSERC/RGPIN 418372-17. Numerical simulations were performed on the Béluga supercomputer at McGill University, under the auspices of Calcul Québec and Compute Canada. The author is grateful for discussions with Peter Bartello and for the constructive comments of Rich Rotunno, Tina Chow, and two anonymous reviewers.

APPENDIX

Parcel-Based Bulk Entrainment and Detrainment Diagnoses

Like other bulk formulations (e.g., SC95), ours enforces the linear-mixing hypothesis, where the mixing of two air parcels with different conserved properties leads to a proportionate change in the conserved property, depending on the mass fraction of each parcel contained in the mixture. Applying this assumption, the prognostic equation for a moist conserved variable ϕ within a homogeneous air parcel is

$$\frac{D\phi_p}{Dt} = \varepsilon(\phi_e - \phi_p), \quad \text{(A1)}$$

where ϕ_p is the value within the parcel, ϕ_e is the value within the environment, and ε is the fractional entrainment rate (in units of s^{-1}).

To calculate fractional entrainment, we evaluate (A1) along Lagrangian parcel trajectories, where the only process that can change ϕ_p is entrainment. Passive-tracer concentrations, which are conserved even in precipitating flows, are taken as ϕ. At each model output time, all parcels that qualify as cores (again defined as saturated, ascending, and positively buoyant relative to the local y average) are analyzed. For each one, ϕ_p is defined as the parcel value of ϕ, and ϕ_e is taken as the y average of all noncore grid points, linearly interpolated to the same x, z position as the parcel. Applying (A1), we then calculate $\varepsilon_{co}(n, \mathbf{x}, t)$, where n is the parcel identification number, $\mathbf{x}$ is the parcel position, and t is the time.

A similar calculation is undertaken to obtain δ. At each model output time, all parcels that do not qualify as cores, but coexist with other core grid points at the same x, z location, are analyzed. For each such parcel, ϕ_p is assigned the parcel value of ϕ, and ϕ_e is taken as the *core* average at that same x, z location. The entrainment of core air into the noncore parcel, henceforth termed $\varepsilon_{nc}(n, \mathbf{x}, t)$, is then determined using (A1).

Given our goal of determining δ_{co} rather than ε_{nc}, it is necessary to relate these two quantities. To that end, the fractional Lagrangian time derivatives of the core and noncore parcel masses may be written

$$\frac{1}{m_{co}}\frac{Dm_{co}}{Dt} = \varepsilon_{co} - \delta_{co}, \quad \text{(A2)}$$

$$\frac{1}{m_{nc}}\frac{Dm_{nc}}{Dt} = \varepsilon_{nc} - \delta_{nc}, \quad \text{(A3)}$$

where m is parcel mass, δ is the fractional detrainment rate (in units of s^{-1}), and the subscripts "co" and "nc" refer to core and noncore parcels. While (A2) addresses entrainment of noncore air into, and detrainment out of, the core parcels, (A3) describes the entrainment of core air into, and detrainment out of, the noncore parcels. Converting the Lagrangian derivatives of (A2) by (A3) into differential form, and dividing (A2) by (A3), gives

$$\frac{m_{nc}}{m_{co}}\frac{\delta m_{co}}{\delta m_{nc}} = \frac{\varepsilon_{co} - \delta_{co}}{\varepsilon_{nc} - \delta_{nc}}. \quad \text{(A4)}$$

Mass conservation requires that any change in m_{co} must be balanced by an equal and opposite change in m_{nc}, which reduces (A4) to

$$-\frac{m_{nc}}{m_{co}} = \frac{\varepsilon_{co} - \delta_{co}}{\varepsilon_{nc} - \delta_{nc}}, \quad \text{(A5)}$$

or, equivalently,

$$-\frac{\rho_{nc}A_{nc}\Delta z_{nc}}{\rho_{co}A_{co}\Delta z_{co}} = \frac{\varepsilon_{co} - \delta_{co}}{\varepsilon_{nc} - \delta_{nc}} \quad \text{(A6)}$$

where ρ is the density, A is the horizontal area, and Δz is the depth of the parcel. We make three approximations to simplify (A6): (i) for a pure core-detrainment event, $\varepsilon_{co} = \delta_{nc} = 0$, (ii) given that cloud buoyancies are generally small, $\rho_{nc}/\rho_{co} \approx 1$, and (iii) all mass changes are realized by changes in parcel horizontal area, such that $\Delta z_{nc} = \Delta z_{co}$. While these assumptions make the resulting value of δ_{co} more uncertain than the corresponding ε_{co}, they result in an attractively simple form of δ_{co}:

$$\delta_{co} \approx \varepsilon_{nc}\frac{A_{nc}}{A_{co}}. \quad \text{(A7)}$$

At each model output time, ε_{co} is calculated for all core parcels, and ε_{nc} is calculated for all noncore parcels. To obtain δ_{co}, we calculate A_{nc} and A_{co} as the respective fractions of core and noncore grid points in y, linearly interpolated to the parcel's x–z position. Both ε_{nc} and δ_{co} are only calculated in locations where $A_{co} \geq 0$, or else no core material is available for detrainment and (A7) is invalid. The resulting ε_{co} and δ_{co} values are then binned onto a uniform x, z grid with a spacing of 500 m in the horizontal and 200 m in the vertical. In each grid box, averages of ε_{co} and δ_{co} are taken over all parcels traversing that box within the analysis time window. The results are then expressed as 2D (x–z) time-averaged maps of ε_{co} and δ_{co}.

REFERENCES

Beare, R. J., 2014: A length scale defining partially-resolved boundary-layer turbulence simulations. *Bound.-Layer Meteor.*, **151**, 39–55, https://doi.org/10.1007/s10546-013-9881-3.

Bechtold, P., N. Semane, P. Lopez, J.-P. Chaboureau, A. Beljaars, and N. Bormann, 2014: Representing equilibrium and nonequilibrium convection in large-scale models. *J. Atmos. Sci.*, **71**, 734–753, https://doi.org/10.1175/JAS-D-13-0163.1.

Betts, A. K., 1975: Parametric interpretation of trade-wind cumulus budget studies. *J. Atmos. Sci.*, **32**, 1934–1945, https://doi.org/10.1175/1520-0469(1975)032<1934:PIOTWC>2.0.CO;2.

Boutle, I. A., J. E. J. Eyre, and A. P. Lock, 2014: Seamless stratocumulus simulation across the turbulent gray zone. *Mon. Wea. Rev.*, **142**, 1655–1668, https://doi.org/10.1175/MWR-D-13-00229.1.

Bryan, G. H., and J. M. Fritsch, 2002: A benchmark simulation for moist nonhydrostatic models. *Mon. Wea. Rev.*, **130**, 2917–2928, https://doi.org/10.1175/1520-0493(2002)130<2917:ABSFMN>2.0.CO;2.

——, and R. Rotunno, 2009: The maximum intensity of tropical cyclones in axisymmetric numerical model simulations. *Mon. Wea. Rev.*, **137**, 1770–1789, https://doi.org/10.1175/2008MWR2709.1.

——, J. C. Wyngaard, and J. M. Fritsch, 2003: Resolution requirements for the simulation of deep moist convection. *Mon. Wea. Rev.*, **131**, 2394–2416, https://doi.org/10.1175/1520-0493(2003)131<2394:RRFTSO>2.0.CO;2.

Bullock, O. R., K. Alapaty, J. A. Herwehe, and J. S. Kain, 2015: A dynamically computed convective time scale for the Kain-Fritsch convective parameterization scheme. *Mon. Wea. Rev.*, **143**, 2105–2120, https://doi.org/10.1175/MWR-D-14-00251.1.

Cannon, D. J., 2012: The influence of embedded convection on orographic precipitation. Ph.D. thesis, Dept. of Meteorology, University of Reading, 220 pp.

Chow, F. K., C. Schär, N. Ban, K. A. Lundquist, L. Schlemmer, and X. Shi, 2019: Crossing multiple gray zones in the transition from mesoscale to microscale simulation over complex terrain. *Atmosphere*, **10**, 274, https://doi.org/10.3390/atmos10050274.

Clark, A. J., and Coauthors, 2012: An overview of the 2010 hazardous weather testbed experimental forecast program spring experiment. *Bull. Amer. Meteor. Soc.*, **93**, 55–74, https://doi.org/10.1175/BAMS-D-11-00040.1.

Craig, G. C., and A. Dornbrack, 2008: Entrainment in cumulus clouds: What resolution is cloud-resolving? *J. Atmos. Sci.*, **65**, 3978–3988, https://doi.org/10.1175/2008JAS2613.1.

Dai, A., 2006: Precipitation characteristics in eighteen coupled climate models. *J. Climate*, **19**, 4605–4630, https://doi.org/10.1175/JCLI3884.1.

Dawe, J. T., and P. H. Austin, 2011: Interpolation of LES cloud surfaces for use in direct calculations of entrainment and detrainment. *Mon. Wea. Rev.*, **139**, 444–456, https://doi.org/10.1175/2010MWR3473.1.

Deardorff, J. W., 1980: Stratocumulus-capped mixed layers derived from a three-dimensional model. *Bound.-Layer Meteor.*, **18**, 495–527, https://doi.org/10.1007/BF00119502.

de Rooy, W. C., and Coauthors, 2013: Entrainment and detrainment in cumulus convection: An overview. *Quart. J. Roy. Meteor. Soc.*, **139**, 1–19, https://doi.org/10.1002/qj.1959.

Dirmeyer, P. A., and Coauthors, 2012: Simulating the diurnal cycle of rainfall in global climate models: Resolution versus parameterization. *Climate Dyn.*, **39**, 399–418, https://doi.org/10.1007/s00382-011-1127-9.

Durran, D. R., 1990: Mountains waves and downslope winds. *Atmospheric Processes over Complex Terrain*, *Meteor. Monogr.*, No. 45, Amer. Meteor. Soc, 59–81, https://doi.org/10.1007/978-1-935704-25-6_4.

——, and J. B. Klemp, 1982: On the effects of moisture on the Brunt-Väisälä frequency. *J. Atmos. Sci.*, **39**, 2152–2158, https://doi.org/10.1175/1520-0469(1982)039<2152:OTEOMO>2.0.CO;2.

——, J. A. Weyn, and M. Q. Menchaca, 2017: Practical considerations for computing dimensional spectra from gridded data. *Mon. Wea. Rev.*, **145**, 3901–3910, https://doi.org/10.1175/MWR-D-17-0056.1.

Field, P. R., and Coauthors, 2017: Exploring the convective grey zone with regional simulations of a cold air outbreak. *Quart. J. Roy. Meteor. Soc.*, **143**, 2537–2555, https://doi.org/10.1002/qj.3105.

Fiori, E., A. Parodi, and F. Siccardi, 2010: Turbulence closure parameterization and grid spacing effects in simulated supercell storms. *J. Atmos. Sci.*, **67**, 3870–3890, https://doi.org/10.1175/2010JAS3359.1.

Fuhrer, O., and C. Schär, 2005: Embedded cellular convection in moist flow past topography. *J. Atmos. Sci.*, **62**, 2810–2828, https://doi.org/10.1175/JAS3512.1.

Hanley, K. E., R. S. Plant, T. H. M. Stein, R. J. Hogan, J. C. Nicol, H. W. Lean, C. Halliwell, and P. A. Clark, 2015: Mixing-length controls on high-resolution simulations of convective storms. *Quart. J. Roy. Meteor. Soc.*, **141**, 272–284, https://doi.org/10.1002/qj.2356.

Hong, S.-Y., Y. Noh, and J. Dudhia, 2006: A new vertical diffusion package with an explicit treatment of entrainment processes. *Mon. Wea. Rev.*, **134**, 2318–2341, https://doi.org/10.1175/MWR3199.1.

Honnert, R., 2016: Representation of the grey zone of turbulence in the atmospheric boundary layer. *Adv. Sci. Res.*, **13**, 63–67, https://doi.org/10.5194/asr-13-63-2016.

——, V. Masson, and F. Couvreux, 2011: A diagnostic for evaluating the representation of turbulence in atmospheric models at the kilometric scale. *J. Atmos. Sci.*, **68**, 3112–3131, https://doi.org/10.1175/JAS-D-11-061.1.

Jiang, Q., 2003: Moist dynamics and orographic precipitation. *Tellus*, **55A**, 301–316, https://doi.org/10.1034/J.1600-0870.2003.00025.X.

Kain, J. S., 2004: The Kain–Fritsch convective parameterization: An update. *J. Appl. Meteor.*, **43**, 170–181, https://doi.org/10.1175/1520-0450(2004)043<0170:TKCPAU>2.0.CO;2.

Kirshbaum, D. J., 2013: On thermally forced circulations over heated terrain. *J. Atmos. Sci.*, **70**, 1690–1709, https://doi.org/10.1175/JAS-D-12-0199.1.

——, and D. R. Durran, 2004: Factors governing cellular convection in orographic precipitation. *J. Atmos. Sci.*, **61**, 682–698, https://doi.org/10.1175/1520-0469(2004)061<0682:FGCCIO>2.0.CO;2.

——, and R. B. Smith, 2009: Orographic precipitation in the tropics: Large-eddy simulations and theory. *J. Atmos. Sci.*, **66**, 2559–2578, https://doi.org/10.1175/2009JAS2990.1.

——, B. Adler, N. Kalthoff, C. Barthlott, and S. Serafin, 2018: Moist orographic convection: Physical mechanisms and links to surface-exchange processes. *Atmosphere*, **9**, 80, https://doi.org/10.3390/atmos9030080.

Langhans, W., J. Schmidli, and C. Schär, 2012: Bulk convergence of cloud-resolving simulations of moist convection over complex terrain. *J. Atmos. Sci.*, **69**, 2207–2228, https://doi.org/10.1175/JAS-D-11-0252.1.

Leonard, A., 1975: Energy cascade in large-eddy simulations of turbulent fluid flows. *Advances in Geophysics*, Vol. 18A, Academic Press, 237–248, https://doi.org/10.1016/S0065-2687(08)60464-1.

Miglietta, M. M., and R. Rotunno, 2009: Numerical simulations of conditionally unstable flows over a ridge. *J. Atmos. Sci.*, **66**, 1865–1885, https://doi.org/10.1175/2009JAS2902.1.

——, and ——, 2012: Application of theory to simulations of observed cases of orographically forced convective rainfall. *Mon. Wea. Rev.*, **140**, 3039–3053, https://doi.org/10.1175/MWR-D-11-00253.1.

Moeng, C.-H., P. P. Sullivan, M. F. Khairoutdinov, and D. A. Randall, 2010: A mixed scheme for subgrid-scale fluxes in cloud-resolving models. *J. Atmos. Sci.*, **67**, 3692–3705, https://doi.org/10.1175/2010JAS3565.1.

Morrison, H., G. Thompson, and V. Tatarskii, 2009: Impact of cloud microphysics on the development of trailing stratiform precipitation in a simulated squall line: Comparison of one- and two-moment schemes. *Mon. Wea. Rev.*, **137**, 991–1007, https://doi.org/10.1175/2008MWR2556.1.

Panosetti, D., S. Böing, L. Schlemmer, and J. Schmidli, 2016: Idealized large-eddy and convection-resolving simulations of moist convection over mountainous terrain. *J. Atmos. Sci.*, **73**, 4021–4041, https://doi.org/10.1175/JAS-D-15-0341.1.

——, L. Schlemmer, and C. Schär, 2019: Bulk and structural convergence at convection-resolving scales in real-case simulations of summertime moist convection over land. *Quart. J. Roy. Meteor. Soc.*, **145**, 1427–1443, https://doi.org/10.1002/qj.3502.

Purnell, D. J., and D. J. Kirshbaum, 2018: Synoptic control over orographic precipitation distributions during the Olympics Mountains experiment (OLYMPEX). *Mon. Wea. Rev.*, **146**, 1023–1044, https://doi.org/10.1175/MWR-D-17-0267.1.

Ricard, D., C. Lac, S. Riette, R. Legrand, and A. Mary, 2013: Kinetic energy spectra characteristics of two convection-permitting limited-area models AROME and Meso-NH. *Quart. J. Roy. Meteor. Soc.*, **139**, 1327–1341, https://doi.org/10.1002/qj.2025.

Romps, D. M., 2010: A direct measure of entrainment. *J. Atmos. Sci.*, **67**, 1908–1927, https://doi.org/10.1175/2010JAS3371.1.

Rougier, J., D. M. H. Sexton, J. M. Murphy, and D. Stainforth, 2009: Analyzing the climate sensitivity of the HadSM3 climate model using ensembles from different but related experiments. *J. Climate*, **22**, 3540–3557, https://doi.org/10.1175/2008JCLI2533.1.

Rousseau-Rizzi, R., D. J. Kirshbaum, and M. K. Yau, 2017: Initiation of deep convection over an idealized mesoscale convergence line. *J. Atmos. Sci.*, **74**, 835–853, https://doi.org/10.1175/JAS-D-16-0221.1.

Schwitalla, T., H.-S. Bauer, V. Wulfmeyer, and G. Zängl, 2008: Systematic errors of QPF in low-mountain regions as revealed by MM5 simulations. *Meteor. Z.*, **17**, 903–919, https://doi.org/10.1127/0941-2948/2008/0338.

Shi, X., H. L. Hagen, F. K. Chow, G. H. Bryan, and R. L. Street, 2018: Large-eddy simulation of the stratocumulus-capped boundary layer with explicit filtering and reconstruction turbulence modeling. *J. Atmos. Sci.*, **75**, 611–637, https://doi.org/10.1175/JAS-D-17-0162.1.

——, F. K. Chow, R. L. Street, and G. H. Bryan, 2019a: Key elements of turbulence closures for simulating deep convection at kilometer-scale resolution. *J. Adv. Model. Earth Syst.*, **11**, 818–838, https://doi.org/10.1029/2018MS001446.

——, R. M. Enriquez, R. L. Street, G. H. Bryan, and F. K. Chow, 2019b: An implicit algebraic turbulence closure scheme for atmospheric boundary layer simulation. *J. Atmos. Sci.*, **76**, 3367–3386, https://doi.org/10.1175/JAS-D-18-0375.1.

Shin, H. H., and S.-Y. Hong, 2013: Analysis of resolved and parameterized vertical transports in convective boundary layers at gray-zone resolutions. *J. Atmos. Sci.*, **70**, 3248–3261, https://doi.org/10.1175/JAS-D-12-0290.1.

Siebesma, A. P., and J. W. M. Cuijpers, 1995: Evaluation of parametric assumptions for shallow cumulus convection. *J. Atmos. Sci.*, **52**, 650–666, https://doi.org/10.1175/1520-0469(1995)052<0650:EOPAFS>2.0.CO;2.

Skamarock, W. C., 2004: Evaluating mesoscale NWP models using kinetic energy spectra. *Mon. Wea. Rev.*, **132**, 3019–3032, https://doi.org/10.1175/MWR2830.1.

Smagorinsky, J., 1963: General circulation experiments with the primitive equations. Part I: The basic experiment. *Mon. Wea. Rev.*, **91**, 99–164, https://doi.org/10.1175/1520-0493(1963)091<0099:GCEWTP>2.3.CO;2.

Smith, R. B., 1989: Hydrostatic flow over mountains. *Advances in Geophysics*, Vol. 31, Academic Press, 1–41, https://doi.org/10.1016/S0065-2687(08)60052-7.

Soderholm, B., B. Ronalds, and D. J. Kirshbaum, 2014: The evolution of convective storms initiated by an isolated mountain ridge. *Mon. Wea. Rev.*, **142**, 1430–1451, https://doi.org/10.1175/MWR-D-13-00280.1.

Stirling, A. J., and R. A. Stratton, 2012: Entrainment processes in the diurnal cycle of deep convection over land. *Quart. J. Roy. Meteor. Soc.*, **138**, 1135–1149, https://doi.org/10.1002/qj.1868.

Tang, S. L., and D. J. Kirshbaum, 2020: On the sensitivity of deep-convection initiation to horizontal grid resolution. *Quart. J. Roy. Meteor. Soc.*, **146**, 1085–1105, https://doi.org/10.1002/qj.3726.

Varble, A., H. Morrison, and E. Zipser, 2019: Effects of under-resolved convective dynamics on the evolution of a squall line. *Mon. Wea. Rev.*, **148**, 289–311, https://doi.org/10.1175/MWR-D-19-0187.1.

Verrelle, A., D. Ricard, and C. Lac, 2015: Sensitivity of high-resolution idealized simulations of thunderstorms to horizontal resolution and turbulence parametrization. *Quart. J. Roy. Meteor. Soc.*, **141**, 433–448, https://doi.org/10.1002/qj.2363.

Wang, C., D. Wu, and F. Zhang, 2019: Modification of the convective adjustment time-scale in the Kain-Fritsch eta scheme for the case of weakly forced deep convection over the Tibetan Plateau region. *Quart. J. Roy. Meteor. Soc.*, **145**, 1915–1932, https://doi.org/10.1002/qj.3535.

Warren, R. A., D. J. Kirshbaum, R. S. Plant, and H. W. Lean, 2014: A 'Boscastle-type' quasi-stationary convective system over the UK southwest peninsula. *Quart. J. Roy. Meteor. Soc.*, **140**, 240–257, https://doi.org/10.1002/qj.2124.

Weisman, M. L., W. C. Skamarock, and J. B. Klemp, 1997: The resolution dependence of explicitly modeled convective systems. *Mon. Wea. Rev.*, **125**, 527–548, https://doi.org/10.1175/1520-0493(1997)125<0527:TRDOEM>2.0.CO;2.

Wyngaard, J. C., 2004: Toward numerical modeling in the terra incognita. *J. Atmos. Sci.*, **61**, 1816–1826, https://doi.org/10.1175/1520-0469(2004)061<1816:TNMITT>2.0.CO;2.